

Naval Research Laboratory

Washington, DC 20375-5320



NRL/FR/5340--98-9874

Pulsed Reflection and Transmission for a Dispersive Half Space

ERIC L. MOKOLE
SURENDRA N. SAMADDAR

*Target Characteristics Branch
Radar Division*

June 29, 1998

19980729 014

Approved for public release; distribution is unlimited.

REPORT DOCUMENTATION PAGE

Form Approved
OMB No. 0704-0188

Public reporting burden for this collection of information is estimated to average 1 hour per response, including the time for reviewing instructions, searching existing data sources, gathering and maintaining the data needed, and completing and reviewing the collection of information. Send comments regarding this burden estimate or any other aspect of this collection of information, including suggestions for reducing this burden, to Washington Headquarters Services, Directorate for Information Operations and Reports, 1215 Jefferson Davis Highway, Suite 1204, Arlington, VA 22202-4302, and to the Office of Management and Budget, Paperwork Reduction Project (0704-0188), Washington, DC 20503.

1. AGENCY USE ONLY (Leave Blank)	2. REPORT DATE	3. REPORT TYPE AND DATES COVERED	
	June 29, 1998	Final	
4. TITLE AND SUBTITLE Pulsed Reflection and Transmission for a Dispersive Half Space			5. FUNDING NUMBERS PE - 61153N TA - LR0210543
6. AUTHOR(S) Eric L. Mokole and Surendra N. Samaddar			
7. PERFORMING ORGANIZATION NAME(S) AND ADDRESS(ES) Naval Research Laboratory Washington, DC 20375-5320			8. PERFORMING ORGANIZATION REPORT NUMBER NRL/FR/5340--98-9874
9. SPONSORING/MONITORING AGENCY NAME(S) AND ADDRESS(ES) Office of Naval Research Arlington, VA 22203			10. SPONSORING/MONITORING AGENCY REPORT NUMBER
11. SUPPLEMENTARY NOTES			
12a. DISTRIBUTION/AVAILABILITY STATEMENT Approved for public release; distribution is unlimited.			12b. DISTRIBUTION CODE
13. ABSTRACT (Maximum 200 words) One-dimensional propagation of a normally incident, pulsed (finite-cycle sine), electromagnetic plane wave on an isotropic, spatially homogeneous, Lorentz half space is investigated analytically. Detailed examinations of the reflected and transmitted fields are made. The inversion integral for the time-domain reflected field is expressed in terms of pole contributions and branch-cut integrals, which are computed numerically; whereas the uniform asymptotic methodology of Oughstun and Sherman is applied to the transmitted field. Only the contributions from the distant saddle points to the transmitted field are studied thoroughly. An example is provided that shows that the reflection and transmission coefficients may not be ignored. Specifically, for Brillouin's choice of the medium's physical parameters, the reflected field has a peak value that is 21% of the incident field's amplitude and that corresponds to a 21% decrease in the main signal (pole contributions) of the transmitted field when the transmission coefficient is unity. This work generalizes past formulations by accounting for reflection from the medium and by addressing how inclusion of frequency-dependent transmission and reflection coefficients affects the fields.			
14. SUBJECT TERMS Pulsed propagation Dispersive media Transmitted field			15. NUMBER OF PAGES 52
			16. PRICE CODE
17. SECURITY CLASSIFICATION OF REPORT UNCLASSIFIED	18. SECURITY CLASSIFICATION OF THIS PAGE UNCLASSIFIED	19. SECURITY CLASSIFICATION OF ABSTRACT UNCLASSIFIED	20. LIMITATION OF ABSTRACT UL

CONTENTS

LIST OF FIGURES	iv
LIST OF TABLES	v
1. INTRODUCTION	1
2. DERIVATION OF FIELDS IN TIME AND FREQUENCY DOMAINS	2
3. EVALUATION OF REFLECTED FIELD	6
3.1 Example of Reflected Field	12
3.2 Early-Time Field Behavior	16
4. EVALUATION OF TRANSMITTED FIELD	20
4.1 Inclusion of Transmission Coefficient in Transmitted Field	20
4.2 Saddle Points of ϕ	22
4.3 Contributions from Distant Saddle Points	26
4.4 Example of Transmitted Field	29
5. SUMMARY AND CONCLUSIONS	32
6. ACKNOWLEDGMENT	33
REFERENCES	33
APPENDIX	37

LIST OF FIGURES

Fig.	Page No.
1 Propagation geometry	3
2 Cut complex plane for Lorentz model of refractive index n	4
3 Closed Jordan contour $C_1 + C_{FU}$ for reflected field when $\tau < 0$	7
4 Closed Jordan contour $C_{FL} + \sum_{n=1}^{13} C_n$ for reflected field when $\tau > 0$	9
5 Behavior of the reflection coefficient R vs carrier frequency ω_c	13
6 Reflected fields at $z = -10^{-5}$ m when boundary is perfectly conducting and when medium is dispersive	15
7 Closed Jordan contour $C_1 + C_{FL}$ for high-frequency reflected field	18
8 Early-time and high-frequency fields vs time	20
9 Sommerfeld precursor and associated functions vs normalized time θ at $z = -10^{-5}$ m in Lorentz medium	31
A1 Refractive index n over the cut complex plane for Brillouin's parameters	43
A2 Cross-sectional views of refractive index for Brillouin's parameters	44
A3 Transmission coefficient T over the cut complex plane for Brillouin's parameters	45
A4 Cross-sectional views of transmission coefficient for Brillouin's parameters	46
A5 Reflection coefficient R over the cut complex plane for Brillouin's parameters	47
A6 Cross-sectional views of reflection coefficient for Brillouin's parameters	48

LIST OF TABLES

Table	Page No.
1 Values of the angles α , ψ , α' , and ψ' along branch cuts	8
2 Eight values of ω_c and associated parameters relevant to Fig. 6	14
3 Comparison of computed values of distant saddle points from two polynomials	24
4 Comparison of computed values of near saddle points from two polynomials	25
A1 Transmission coefficient evaluated at near and distant saddle points	42

PULSED REFLECTION AND TRANSMISSION FOR A DISPERSIVE HALF SPACE

1. INTRODUCTION

This report investigates the one-dimensional (1-D) propagation of normally incident, pulsed, electromagnetic plane waves on a half space that is isotropic, spatially homogeneous, and dispersive. The dispersive nature of the medium is characterized by a singly resonant Lorentz model of the refractive index. Results of previous studies of propagation at optical frequencies are extended to include propagation at nonoptical frequencies through media for which a Lorentz representation is applicable. In the work of Sommerfeld [1], Brillouin [2,3], and Oughstun and Sherman [4-8], the signal is specified on the medium's boundary, and propagation is analyzed inside the Lorentz medium for a constant transmission coefficient of unity. Consequently, these formulations account neither for reflection from the boundary nor for the frequency dependence of the transmission coefficient. The need for a more general formulation that includes frequency-dependent reflection and transmission coefficients is justified by rigorous and plausibility arguments. Not only does the approach delineated herein include reflection, but it also provides the framework for addressing sources that are external to the medium. Further, the ability to determine the reflected field has the advantage of providing a diagnostic capability for learning about the medium through the behavior of the reflected signal. The motivation for this study stems from a desire to apply the uniform asymptotic methodology of Oughstun and Sherman to propagation at radio frequencies. Specifically, one would like to apply the uniform asymptotic approach to two radar problems: (1) transitionospheric propagation at frequencies between 10 MHz and 3 GHz and (2) low-altitude propagation above the sea surface for frequencies between 10 MHz and 100 GHz. Of course, the relations among the physical parameters that describe these media are different from their relationships at optical frequencies. A byproduct of this analysis is its applicability to transmission of short-pulse signals by ultrawideband (UWB) radars [9], a recent area of active research [10-14].

In Section 2, the problem is stated, and the reflected and transmitted fields in the frequency domain for an arbitrary pulsed plane wave are given. Integral expressions of the corresponding temporal fields are obtained in a straightforward manner by taking the inverse transform of the frequency-domain fields; and the geometry, associated with the transforms and with the analytical model for the refractive index n of a singly resonant Lorentz medium, is discussed. In the Lorentz model of the medium, the resonance frequency ω_0 is assumed to exceed the absorption frequency δ . The remainder of the report addresses the evaluation of the reflected and transmitted fields for an incident pulsed plane wave that is a sine function with a finite number of cycles.

An exact expression for the reflected field is obtained in Section 3. This expression is then reformulated to provide more numerically tractable results, which are evaluated for Brillouin's choice of the Lorentz medium parameters for several values of the sine function's carrier frequency ω_c . These results are used to obtain a physical understanding of the impact of the dispersive

medium on the reflected field. In particular, one observes the origin of the broadening of the reflected field. Moreover, the authors demonstrate that the reflected field is significant and should not be ignored, even at optical frequencies for certain ranges of ω_c and ω_0 . In addition, the early-time and high-frequency fields are derived and compared, and the high-frequency field is shown to be a generalization of an earlier result by Colby [15].

In Section 4, the time-domain transmitted field is treated under the uniform asymptotic methodology developed in Ref. 4 for evaluating the solution in the far field. In this approach, the observation points are taken sufficiently far into the Lorentz medium to guarantee the asymptotic representation of the field. As mentioned earlier, this analysis generalizes optical formulations of propagation relative to a Lorentz medium to electromagnetic propagation through that medium by including a frequency-dependent transmission coefficient. Hence the extension is applicable in situations where the frequency dependence of the transmission coefficient is important, such as propagation at microwave and millimeter-wave frequencies, propagation involving ultrawideband signals, or optical propagation for certain ranges of the physical parameters. The advantage of Oughstun and Sherman's methodology is that it partitions the inversion integral into three basic components, which are handled separately. The components roughly correspond to contributions from saddle points far from the origin (Sommerfeld precursor), from saddle points close to the origin (Brillouin precursor), and from poles of the inversion integrand (main signal). The impact of the frequency-dependent transmission coefficient is demonstrated through detailed analysis of the Sommerfeld precursor and a heuristic discussion of the main signal. Since the objective here is to establish the credibility of including the transmission coefficient for propagation through a Lorentz medium, complete treatments of the Brillouin precursor and the main signal are not undertaken.

Since the transmitted field depends crucially on the behavior of the saddle points of the inversion integral's generalized phase, the eighth-degree polynomial [4,8] of which the saddle points are roots is corrected. Although the polynomial has errors that lead to incorrect values for the saddle points, no errors are found in any calculations involving the saddle points in Refs. 4 and 8. Moreover, for Brillouin's values of the physical parameters, the contributions of the distant saddle points to the transmitted field are determined, the effect of including the transmission coefficient is discussed, and aspects of the transmitted field are compared to the reflected field. In particular, the peak value of the reflected field is shown to be 21% of the incident field's amplitude, and the component of the transmitted field associated with the poles of the inversion integral (main signal) is heuristically argued to be 79% of the field obtained when the transmission coefficient is unity. The purpose of this example is to demonstrate that the reflection and transmission coefficients should not be ignored. Lastly, the Appendix presents detailed investigations of the refractive index, reflection coefficient, and transmission coefficient over the complex plane. In addition to analytical arguments, two-dimensional (2-D) and three-dimensional (3-D) graphs are used to characterize the behavior of each quantity.

2. DERIVATION OF FIELDS IN TIME AND FREQUENCY DOMAINS

A pulsed plane wave $\vec{E}^i(z, t)$, traveling in the positive z direction in free space ($z < 0$), is normally incident on the dispersive half space ($z \geq 0$) at observation time $t = 0$ (Fig. 1). The fields in both half spaces satisfy Maxwell's equations

$$\frac{\partial E_y}{\partial z} = \mu_0 \frac{\partial H_x}{\partial t} \quad \text{and} \quad \frac{\partial H_x}{\partial z} = \frac{\partial D_y}{\partial t}. \quad (1)$$

Let $\hat{E}_y(z, \omega)$, $\hat{D}_y(z, \omega)$, and $\hat{H}_x(z, \omega)$ be the complex Fourier transforms of $E_y(z, t)$, $D_y(z, t)$, and $H_x(z, t)$, respectively, for the complex variable ω . If G represents any of the temporal functions and \hat{G} is the associated Fourier transform, the complex Fourier transform pair is

$$\hat{G}(\omega) = \frac{1}{2\pi} \int_{-\infty}^{+\infty} G(t) e^{it\omega} dt, \quad G(t) = \int_C \hat{G}(\omega) e^{-it\omega} d\omega. \quad (2)$$

The contour C is the horizontal line in the complex ω plane that runs from $-\infty + ia$ to $+\infty + ia$. The real constant a is chosen so that all of the integrand's singularities lie below the line and so that $e^{-at}G(t)$ is absolutely integrable for all of the fields. The existence of the transform pair is guaranteed for any positive a satisfying these conditions.

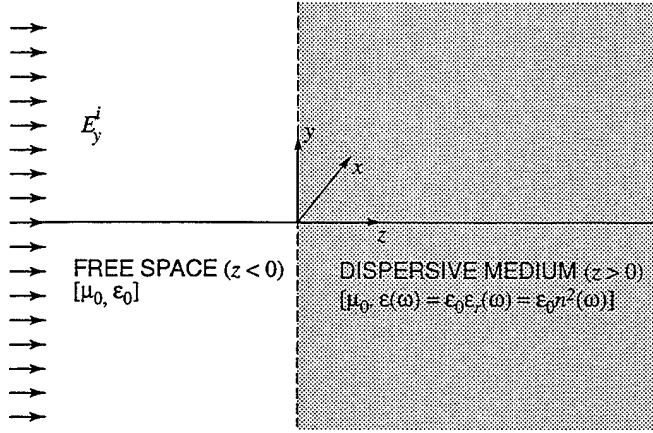


Fig. 1 – Geometry and specified coordinate frame for a pulsed plane wave $E_y^i(z, t)$ in free space ($z < 0$) that depends only on its propagation direction z and is normally incident on the dispersive medium at $z = 0$. The positive x direction points into the paper, and the dispersive medium occupies the half space $z > 0$. Free space is characterized by the permittivity ϵ_0 and permeability μ_0 , and the dispersive medium is defined by the free-space permeability μ_0 and the frequency-dependent relative permittivity $\epsilon_r(\omega)$. The quantity n is the dispersive medium's refractive index.

Transforming Eqs. (1) and substituting $\hat{D}_y(z, \omega) = \epsilon(\omega)\hat{E}_y(z, \omega)$ yield the one dimensional Helmholtz equation in the Fourier domain for the electric field,

$$\frac{\partial^2 \hat{E}_y}{\partial z^2} + k^2 \hat{E}_y = 0, \quad (3)$$

where $k^2(\omega) = \mu_0\epsilon(\omega)\omega^2$. The magnetic field is related to the electric field through

$$\hat{H}_x = \frac{i}{\mu_0\omega} \frac{\partial \hat{E}_y}{\partial z}. \quad (4)$$

The permittivity and wave number are given by

$$\epsilon(\omega) = \begin{cases} \epsilon_0, & z < 0, \\ \epsilon_0 \epsilon_r(\omega), & z > 0, \end{cases} \quad k(\omega) = \begin{cases} k_0(\omega), & z < 0, \\ k(\omega) = k_0(\omega)n(\omega), & z > 0, \end{cases} \quad (5)$$

where $c = 1/\sqrt{\mu_0\epsilon_0}$ is the speed of light in free space, $k_0(\omega) = \omega/c$ is the free-space wave number, ϵ_0 is the permittivity of free space, ϵ_r ($= n^2$) is the permittivity of the dispersive medium, and n is the refractive index of the dispersive medium.

The analytical model for the refractive index of a singly resonant Lorentz medium is [16]

$$n(\omega) = \left[1 - \frac{b^2}{\omega^2 - \omega_0^2 + 2i\delta\omega} \right]^{1/2} = \left[\frac{(\omega - \omega'_+)(\omega - \omega'_-)}{(\omega - \omega_+)(\omega - \omega_-)} \right]^{1/2}. \quad (6)$$

The quantities b , ω_0 , and δ are positive real numbers and represent the plasma frequency, resonance frequency, and damping constant of the medium, respectively. Since $\delta < \omega_0$, the branch points ω'_+ , ω'_- , ω_+ , and ω_- lie in the lower half of the complex ω -plane along the line, $\text{Im}[\omega] = -\delta$, and are given by

$$\begin{aligned} \omega_+ &= \sqrt{\omega_0^2 - \delta^2} - i\delta, \\ \omega_- &= -\sqrt{\omega_0^2 - \delta^2} - i\delta, \\ \omega'_+ &= \sqrt{\omega_1^2 - \delta^2} - i\delta, \\ \omega'_- &= -\sqrt{\omega_1^2 - \delta^2} - i\delta, \end{aligned} \quad (7)$$

where $\text{Re}[\omega] = \omega'$, $\text{Im}[\omega] = \omega''$, and $\omega_1^2 = \omega_0^2 + b^2$ (Fig. 2).

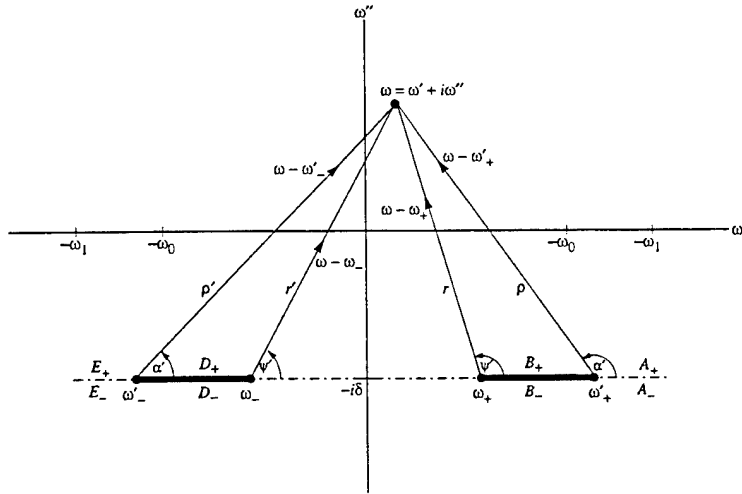


Fig. 2 – Cut complex plane associated with the Lorentz model of the refractive index n for $\delta < \omega_0$, where δ and ω_0 are the attenuation and resonance frequencies, respectively, of the model. The four vectors, $\{\omega - \omega'_-, \omega - \omega_-, \omega - \omega_+, \omega - \omega'_+\}$, represent the vectors from the branch points $\{\omega'_-, \omega_-, \omega_+, \omega'_+\}$ of n to an arbitrary point ω ($= \omega' + i\omega''$) in the complex plane. The magnitudes and angles corresponding to these vectors are $\{\rho', r', r, \rho\}$ and $\{\alpha', \psi', \psi, \alpha\}$, respectively. The branch cuts are the horizontal line segments along $\omega = -i\delta$ that connect ω_+ to ω'_+ and ω_- to ω'_- .

In the following, the superscripts i , r , and t are used to denote the incident, reflected, and transmitted fields, respectively. This investigation assumes that the incident field is an arbitrary

pulsed plane wave with leading edge that first reaches the dispersive medium's boundary ($z = 0$) at time $t = 0$. For $z < 0$ and $t \geq 0$,

$$\hat{E}_y(z, \omega) = \hat{E}_y^i(z, \omega) + \hat{E}_y^r(z, \omega), \quad (8a)$$

$$\hat{H}_x(z, \omega) = \hat{H}_x^i(z, \omega) + \hat{H}_x^r(z, \omega), \quad (8b)$$

$$\hat{E}_y^i(z, \omega) = A(\omega) e^{ik_0(\omega)z}, \quad (8c)$$

$$\hat{E}_y^r(z, \omega) = A(\omega) R(\omega) e^{-ik_0(\omega)z}, \quad (8d)$$

$$\hat{H}_x^i(z, \omega) = -\frac{k_0(\omega)}{\mu_0 \omega} A(\omega) e^{ik_0(\omega)z}, \quad (8e)$$

$$\hat{H}_x^r(z, \omega) = \frac{k_0(\omega)}{\mu_0 \omega} A(\omega) R(\omega) e^{-ik_0(\omega)z}; \quad (8f)$$

and for $z > 0$ and $t \geq 0$,

$$\hat{E}_y(z, \omega) = \hat{E}_y^t(z, \omega) = A(\omega) T(\omega) e^{ik_0(\omega)n(\omega)z}, \quad (9a)$$

$$\hat{H}_x(z, \omega) = \hat{H}_x^t(z, \omega) = -\frac{k_0(\omega)}{\mu_0 \omega} n(\omega) A(\omega) T(\omega) e^{ik_0(\omega)n(\omega)z}. \quad (9b)$$

The reflection (R) and transmission (T) coefficients are given by the usual expressions, and the function A is the complex Fourier transform of $E_y^i(0, t)$. Thus

$$A(\omega) = \frac{1}{2\pi} \int_{-\infty}^{+\infty} E_y^i(0, t) e^{it\omega} dt, \quad (10a)$$

$$R(\omega) = \frac{1 - n(\omega)}{1 + n(\omega)}, \quad (10b)$$

$$T(\omega) = \frac{2}{1 + n(\omega)}. \quad (10c)$$

Inverting Eqs. (8(d)), (8(f)), (9(a)), and (9(b)) yields

$$E_y^r(z, t) = \int_C A(\omega) R(\omega) e^{-i\omega(t+(z/c))} d\omega, \quad (11a)$$

$$E_y^t(z, t) = \int_C A(\omega) T(\omega) e^{i\omega(z/c)[n(\omega) - (ct/z)]} d\omega, \quad (11b)$$

$$H_x^r(z, t) = \frac{1}{\mu_0 c} \int_C A(\omega) R(\omega) e^{-i\omega(t+(z/c))} d\omega, \quad (11c)$$

$$H_x^t(z, t) = -\frac{1}{\mu_0 c} \int_C n(\omega) A(\omega) T(\omega) e^{i\omega(z/c)[n(\omega) - (ct/z)]} d\omega. \quad (11d)$$

These expressions differ from the usual optical solutions in two respects. First, Brillouin, Sommerfeld, and Oughstun specify the incident field on the planar boundary and ignore the reflected field. With the inclusion of the reflected fields, Eqs. (11) are applicable to a wider range of problems, that is, to any electromagnetic propagation problems for which the Lorentz representation of the refractive index is valid. The second difference arises from including the transmission coefficient T in the pertinent integrands. In optical formulations, T corresponds to unity, its limiting value as

ω approaches infinity. That T can vary over the range of integration for nonoptical signals may substantially affect the value of the integrals in Eqs. (11(b)) and (11(d)). The extent to which the inclusion of the transmission coefficient affects the fields is partially answered. Moreover, Eqs. (11) simplify to the optical solutions as the frequency of the incident field approaches optical frequencies.

Because the square root associated with the index of refraction introduces four branch points and the exponents of the transmitted fields (Eqs. (11(b)) and (11(d))) have at least three saddle points, the evaluations of the integrals in Eqs. (11) are nontrivial endeavors. The difficulty in determining the reflected fields is a consequence of having to evaluate integrals along branch cuts. Saddle points are not issues for the reflected fields since neither integrand has saddle points. On the other hand, the integrands associated with the transmitted fields possess three or four saddle points. The number and locations of the saddle points are not affected by the inclusion of R and T and vary with position z of the observation point in the dispersive medium and time t of the observation. The spatiotemporal behavior of the saddle points and their impact on the asymptotic representation of the transmitted field are treated at length in Refs. [4,6,7,8].

Obtaining the time-domain fields in Eqs. (11) requires a more detailed specification of the incident field E_y^i . Of particular interest are modulated sinusoids, $M(t - (z/c)) \sin(\omega_c(t - (z/c)))$, at carrier frequency ω_c . The modulation function M is zero for $t \leq z/c$. Rather than treat an entire class of modulation functions, the reflected and transmitted fields are evaluated specifically for the rectangularly modulated sine. Consequently,

$$E_y^i(z, t) = \sin\left[\omega_c\left(t - \frac{z}{c}\right)\right] \left[U\left(t - \frac{z}{c}\right) - U\left(t - \frac{z}{c} - T_0\right)\right]. \quad (12)$$

The duration T_0 of the modulation is a positive integer multiple of the sine function's period ($T_0 = 2n\pi/\omega_c$ for $n = 1, 2, \dots$), and U is the unit step function

$$U(\tau) = \begin{cases} 0, & \text{for } \tau \leq 0, \\ 1, & \text{for } \tau > 0. \end{cases} \quad (13)$$

Substituting Eq. (12) into Eq. (10a) and taking the complex Fourier transform yield

$$A(\omega) = \begin{cases} \frac{1}{4\pi} e^{i\omega T_0} S(\omega) - \frac{1}{4\pi} S(\omega), & \omega \neq \pm\omega_c, \\ \frac{\pm in}{2\omega_c}, & \omega = \pm\omega_c, \end{cases} \quad (14)$$

where

$$S(\omega) = \frac{1}{\omega - \omega_c} - \frac{1}{\omega + \omega_c}. \quad (15)$$

3. EVALUATION OF REFLECTED FIELD

In this section, the integral for the reflected field E_y^r is investigated, and an exact representation of E_y^r is obtained. Defining $\hat{t} = t + (z/c)$ and substituting Eq. (14) into Eq. (11(a)) yield

$$E_y^r(z, t) = e(z, \hat{t} - T_0) - e(z, \hat{t}), \quad (16)$$

where

$$e(z, \tau) = \frac{1}{4\pi} \int_{-\infty+ia}^{\infty+ia} e^{-i\omega\tau} R(\omega) S(\omega) d\omega. \quad (17)$$

Although the function A is analytic in the complex plane, Eq. (14) permits E_y^r to be written as the difference of two contour integrals that have simple poles at $\pm\omega_c$ on the real axis. Observe that the argument of each integrand's exponent has no saddle points.

For $\tau \leq 0$, the contour C_1 is closed from above by the semicircle C_{FU} (Fig. 3) to ensure that the limit of the integral along C_{FU} goes to zero as F approaches $+\infty$, which is equivalent to invoking causality. Since the interior of contour $C_1 + C_{FU}$ has no poles, the Cauchy Integral Theorem implies that

$$e(z, \tau) = \lim_{F \rightarrow +\infty} \frac{1}{4\pi} \int_{C_1} e^{-i\omega\tau} R(\omega) S(\omega) d\omega = 0. \quad (18)$$

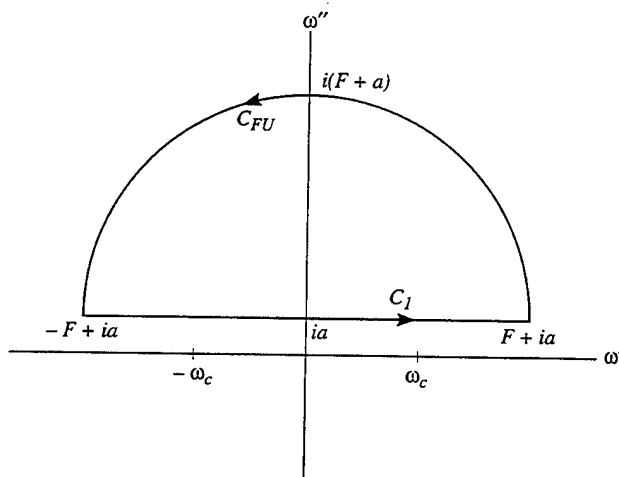


Fig. 3 - Closed Jordan contour $C_1 + C_{FU}$, oriented in the counterclockwise direction, for $e(z, \tau)$ when $\tau < 0$ consists of the line segment C_1 and the semicircle C_{FU} . The line segment goes from $-F + ia$ to $F + ia$, and the semicircle has radius F and center at $\omega = ia$.

Thus far, the branch points of $n(\omega)$ have not played a role; however, they are crucial in determining $e(z, \tau)$ for $\tau > 0$, which is now treated. The associated branch cuts are selected so that contour C_1 is closed from below, thereby guaranteeing the convergence of the inverse transform. In particular, the branch cuts are taken to be the horizontal line segments connecting ω_+ to ω'_+ and ω_- to ω'_- . The branch is specified by making the restrictions

$$\omega - \omega'_+ = pe^{i\alpha}, \quad -\pi < \alpha \leq \pi, \quad (19a)$$

$$\omega - \omega_+ = re^{i\psi}, \quad 0 \leq \psi < 2\pi, \quad (19b)$$

$$\omega - \omega'_- = \rho'e^{i\alpha'}, \quad -\pi < \alpha' \leq \pi, \quad (19c)$$

$$\omega - \omega_- = r'e^{i\psi'}, \quad 0 \leq \psi' < 2\pi. \quad (19d)$$

As indicated by Fig. 2, the angles α , ψ , α' , and ψ' are measured positively in the counterclockwise direction from the positive ω -axis. Table 1 gives values of these angles on the line $\omega = -i\delta$. The "+" and "-" subscripts of locations A , B , C , D , and E denote the top and bottom, respectively, of this line over the indicated regions. Under these restrictions, the refractive index and the reflection

coefficient may be rewritten as

$$n(\omega) = \sqrt{\frac{\rho\rho'}{rr'}} e^{i(\alpha+\alpha'-\psi-\psi')/2} = |n(\omega)| e^{i\arg[n(\omega)]}, \quad (20a)$$

$$R(\omega) = \frac{1 - \frac{\rho\rho'}{rr'}}{1 + \frac{\rho\rho'}{rr'} + 2\sqrt{\frac{\rho\rho'}{rr'}} \cos(\frac{\alpha+\alpha'-\psi-\psi'}{2})} + i \frac{-2\sqrt{\frac{\rho\rho'}{rr'}} \sin(\frac{\alpha+\alpha'-\psi-\psi'}{2})}{1 + \frac{\rho\rho'}{rr'} + 2\sqrt{\frac{\rho\rho'}{rr'}} \cos(\frac{\alpha+\alpha'-\psi-\psi'}{2})}, \quad (20b)$$

where \arg is the argument. See the Appendix for detailed analyses of n and R . The choice of parameters in Eqs. (19) guarantees that n is analytic in the cut plane. In particular, observe that $n(A_+) = n(A_-)$, $n(C_+) = n(C_-)$, and $n(E_+) = n(E_-)$.

Table 1 – Values along the line $\omega = -i\delta$ in the complex plane of the argument of the refractive index n and of the angles $\alpha, \psi, \alpha', \psi'$, measured from this line to line segments connecting the point ω to the branch points $\omega'_+, \omega_+, \omega'_-, \omega_-$, respectively. The letters A, B, C, D, E indicate the disjoint line segments that comprise this line as illustrated in Fig. 2, and the + (–) subscripts denote the top (bottom) of each segment.

Angle Value	A_+	A_-	B_+	B_-	C_+	C_-	D_+	D_-	E_+	E_-
α	0	0	π	$-\pi$	π	$-\pi$	π	$-\pi$	π	$-\pi$
ψ	0	2π	0	2π	π	π	π	π	π	π
α'	0	0	0	0	0	0	0	π	π	$-\pi$
ψ'	0	2π	0	2π	0	2π	π	π	π	π
$\arg[n]$	0	-2π	$\pi/2$	$-5\pi/2$	0	-2π	$-\pi/2$	$-3\pi/2$	0	-2π

The contour C_1 is converted to a Jordan contour C_T by adjoining several contours (Fig. 4): $C_T = C_{FL} + \sum_{n=1}^{13} C_n$. Applying Cauchy's residue theorem and letting $F \rightarrow +\infty$ and $\varepsilon \rightarrow 0+$ simultaneously give

$$e(z, \tau) = -2\pi i [\text{Res}(-\omega_c) + \text{Res}(\omega_c)] - \frac{1}{4\pi} [I_{B_+} + I_{B_-} + I_{D_+} + I_{D_-}], \quad (21)$$

where $\text{Res}(\omega_p)$ is the residue of the integrand at ω_p and

$$I_{B_+} = \lim_{\varepsilon \rightarrow 0+} \int_{C_5} R(\omega) e^{-i\omega\tau} S(\omega) d\omega, \quad (22a)$$

$$I_{B_-} = \lim_{\varepsilon \rightarrow 0+} \int_{C_3} R(\omega) e^{-i\omega\tau} S(\omega) d\omega, \quad (22b)$$

$$I_{D_+} = \lim_{\varepsilon \rightarrow 0+} \int_{C_9} R(\omega) e^{-i\omega\tau} S(\omega) d\omega, \quad (22c)$$

$$I_{D_-} = \lim_{\varepsilon \rightarrow 0+} \int_{C_{11}} R(\omega) e^{-i\omega\tau} S(\omega) d\omega. \quad (22d)$$

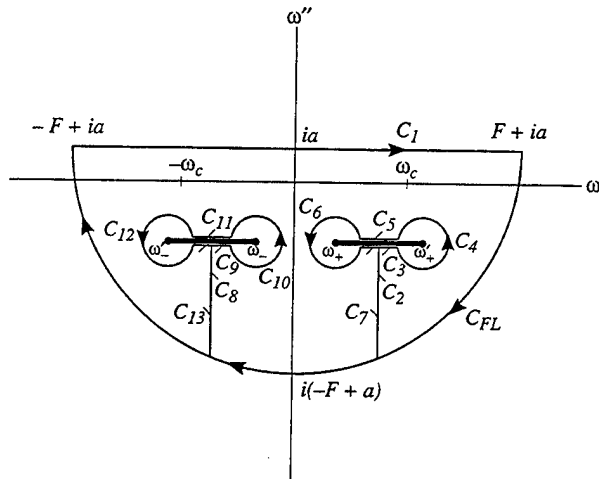


Fig. 4 – Closed Jordan contour $C_{FL} + \sum_{n=1}^{13} C_n$, oriented in the clockwise direction, for $e(z, \tau)$ when $\tau > 0$ consists of five horizontal line segments $\{C_1, C_3, C_5, C_9, C_{11}\}$, four vertical line segments $\{C_2, C_7, C_8, C_{13}\}$, four circles $\{C_4, C_6, C_{10}, C_{12}\}$ of radius ε , and one semicircle C_{FL} of radius F . The four circles are centered about the branch points $\{\omega'_-, \omega'_-, \omega'_+, \omega'_+\}$, the horizontal line segments are the tops and bottoms of the two branch cuts, and the semicircle is centered at $\omega = ia$.

To obtain an expression for $e(z, \tau)$, the four line integrals in Eqs. (22) must be evaluated, and the two residues must be obtained. Before evaluating the line integrals, define two more quantities:

$$\omega_2 = \sqrt{\omega_0^2 - \delta^2} \quad \text{and} \quad \omega_3 = \sqrt{\omega_1^2 - \delta^2}. \quad (23)$$

Since $\omega_1^2 = \omega_0^2 + b^2$, $\omega_3 > \omega_2$.

Along the top of the right cut, which corresponds to the region B_+ in Fig. 2, parameterize C_5 as: $\omega = r + \omega_+ = r + \omega_2 - i\delta$ with magnitude r running from $\omega_3 - \omega_2 - \varepsilon$ to ε . The remaining magnitudes of Eqs. (19) are

$$\begin{aligned} \rho &= \omega_3 - \omega_2 - r, \\ r' &= r + 2\omega_2, \\ \rho' &= \omega_3 + \omega_2 + r. \end{aligned} \quad (24)$$

From Table 1, $\alpha = \pi$ and $\psi = \alpha' = \psi' = 0$. Consequently, Eqs. (20) become

$$n(\omega) = i \left[\frac{(\omega_3 + \omega_2 + r)(\omega_3 - \omega_2 - r)}{r(r + 2\omega_2)} \right]^{1/2}, \quad (25a)$$

$$R(\omega) = \frac{\sqrt{r(r + 2\omega_2)} - i\sqrt{(\omega_3 + \omega_2 + r)(\omega_3 - \omega_2 - r)}}{\sqrt{r(r + 2\omega_2)} + i\sqrt{(\omega_3 + \omega_2 + r)(\omega_3 - \omega_2 - r)}}. \quad (25b)$$

After substituting Eq. (25(b)) into Eq. (22(a)) and taking the limit, one obtains Eq. (26(a)) as the expression for I_{B_+} . The integral for I_{B_-} is gotten by the same parameterization. On the other

hand, along the left cut use the parameterization: $\omega = -r' + \omega_- = -r' - \omega_2 - i\delta$ with r' running from ε to $\omega_3 - \omega_2 - \varepsilon$. Consequently,

$$I_{B+} = -e^{-(\delta+i\omega_2)\tau} \int_0^{\omega_3-\omega_2} e^{-ir\tau} \left[\frac{1}{r + \omega_2 - \omega_c - i\delta} - \frac{1}{r + \omega_2 + \omega_c - i\delta} \right] R(\omega) dr, \quad (26a)$$

$$I_{B-} = e^{-(\delta+i\omega_2)\tau} \int_0^{\omega_3-\omega_2} e^{-ir\tau} \left[\frac{1}{r + \omega_2 - \omega_c - i\delta} - \frac{1}{r + \omega_2 + \omega_c - i\delta} \right] R^*(\omega) dr, \quad (26b)$$

$$I_{D+} = e^{-(\delta-i\omega_2)\tau} \int_0^{\omega_3-\omega_2} e^{ir\tau} \left[\frac{1}{r + \omega_2 + \omega_c + i\delta} - \frac{1}{r + \omega_2 - \omega_c + i\delta} \right] R^*(\omega) dr, \quad (26c)$$

$$I_{D-} = -e^{-(\delta-i\omega_2)\tau} \int_0^{\omega_3-\omega_2} e^{-ir\tau} \left[\frac{1}{r + \omega_2 + \omega_c + i\delta} - \frac{1}{r + \omega_2 - \omega_c + i\delta} \right] R(\omega) dr. \quad (26d)$$

Observe that $I_{D+} = [I_{B+}]^*$ and $I_{D-} = [I_{B-}]^*$. Therefore, $I_{B+} + I_{B-} + I_{D+} + I_{D-} = 2\text{Re}\{I_{B+} + I_{B-}\}$, so that the field is expressed in terms of integrals along the right branch cut only. After some algebra,

$$I_{B+} + I_{B-} + I_{D+} + I_{D-} = \text{Re} \left\{ \frac{8i}{b^2} e^{-(\delta+i\omega_2)\tau} \int_0^{\omega_3-\omega_2} e^{-ir\tau} \left[\frac{1}{r + \omega_2 - \omega_c - i\delta} - \frac{1}{r + \omega_2 + \omega_c - i\delta} \right] \sqrt{r(r+2\omega_2)(b^2 - r(r+2\omega_2))} dr. \right\} \quad (27)$$

It remains to calculate the residues at $\pm\omega_c$. First,

$$\text{Res}(\omega_c) = \frac{1}{4\pi} R(\omega_c) e^{-i\omega_c\tau}. \quad (28)$$

Since $n(-\omega) = [n(\omega^*)]^*$, $R(-\omega_c) = [R(\omega_c^*)]^*$, which implies that $\text{Res}(-\omega_c) = -[\text{Res}(\omega_c)]^*$. Combining this result with Eq. (28) yields

$$-2\pi i [\text{Res}(-\omega_c) + \text{Res}(\omega_c)] = \cos(\omega_c\tau) \text{Im}[R(\omega_c)] - \sin(\omega_c\tau) \text{Re}[R(\omega_c)] \quad (29)$$

as the contribution of the poles to $e(z, \tau)$.

Equation (18) and the substitution of Eqs. (27) and (29) into Eq. (21) imply that

$$e(z, \tau) = \left(\cos(\omega_c\tau) \text{Im}[R(\omega_c)] - \sin(\omega_c\tau) \text{Re}[R(\omega_c)] \right. \\ \left. - \frac{2}{\pi b^2} \text{Re} \left\{ ie^{-(\delta+i\omega_2)\tau} \int_0^{\omega_3-\omega_2} e^{-ir\tau} \left[\frac{1}{r + \omega_2 - \omega_c - i\delta} - \frac{1}{r + \omega_2 + \omega_c - i\delta} \right] \right. \right. \\ \left. \left. \times \sqrt{r(r+2\omega_2)(b^2 - r(r+2\omega_2))} dr \right\} \right) U(\tau). \quad (30)$$

To perform numerical computations, it is desirable to recast this expression. After more algebra, one obtains

$$e(z, \tau) = \left(\cos(\omega_c\tau) \text{Im}[R(\omega_c)] - \sin(\omega_c\tau) \text{Re}[R(\omega_c)] \right. \\ \left. - \frac{2}{\pi b^2} e^{-\delta\tau} [\sin(\omega_2\tau) I_1(\tau) - \cos(\omega_2\tau) I_2(\tau)] \right) U(\tau), \quad (31)$$

where

$$I_1(\tau) = \int_0^{\omega_3 - \omega_2} N_1(r, \tau) [r(r + 2\omega_2)(b^2 - r(r + 2\omega_2))]^{1/2} dr, \quad (32a)$$

$$I_2(\tau) = \int_0^{\omega_3 - \omega_2} N_2(r, \tau) [r(r + 2\omega_2)(b^2 - r(r + 2\omega_2))]^{1/2} dr, \quad (32b)$$

$$N_1(r, \tau) = \frac{2\omega_c [(r + \omega_2)^2 - \omega_c^2 - \delta^2] \cos(r\tau) + 4\omega_c \delta(r + \omega_2) \sin(r\tau)}{[(r + \omega_2 - \omega_c)^2 + \delta^2][(r + \omega_2 + \omega_c)^2 + \delta^2]}, \quad (32c)$$

$$N_2(r, \tau) = \frac{4\omega_c \delta(r + \omega_2) \cos(r\tau) - 2\omega_c [(r + \omega_2)^2 - \omega_c^2 - \delta^2] \sin(r\tau)}{[(r + \omega_2 - \omega_c)^2 + \delta^2][(r + \omega_2 + \omega_c)^2 + \delta^2]}. \quad (32d)$$

Evaluation of the real and imaginary parts of $R(\omega_c)$ are obtained from substituting the following expressions into Eq. (20(b)):

$$\sqrt{\frac{\rho \rho'}{rr'}} \Big|_{\omega=\omega_c} = \left[\frac{(\omega_c^2 - \omega_1^2)^2 + 4\omega_c^2 \delta^2}{(\omega_c^2 - \omega_0^2)^2 + 4\omega_c^2 \delta^2} \right]^{1/4}, \quad (33a)$$

$$\alpha \Big|_{\omega=\omega_c} = \begin{cases} \pi - \arctan\left(\frac{\delta}{\omega_3 - \omega_c}\right), & 0 < \omega_c < \omega_3 \\ \frac{\pi}{2}, & \omega_c = \omega_3 \\ \arctan\left(\frac{\delta}{\omega_c - \omega_3}\right), & \omega_3 < \omega_c, \end{cases} \quad (33b)$$

$$\alpha' \Big|_{\omega=\omega_c} = \arctan\left(\frac{\delta}{\omega_3 + \omega_c}\right), \quad (33c)$$

$$\psi \Big|_{\omega=\omega_c} = \begin{cases} \pi - \arctan\left(\frac{\delta}{\omega_2 - \omega_c}\right), & 0 < \omega_c < \omega_2 \\ \frac{\pi}{2}, & \omega_c = \omega_2 \\ \arctan\left(\frac{\delta}{\omega_c - \omega_2}\right), & \omega_2 < \omega_c, \end{cases} \quad (33d)$$

$$\psi' \Big|_{\omega=\omega_c} = \arctan\left(\frac{\delta}{\omega_2 + \omega_c}\right). \quad (33e)$$

Finally, substituting Eq. (31) in Eq. (16) yields the following computationally useful, exact expression for the reflected field,

$$\begin{aligned} E_y^r(z, t) = & |R(\omega_c)| \sin(\omega_c \hat{t} - \arg[R(\omega_c)]) [U(\hat{t}) - U(\hat{t} - T_0)] \\ & + \frac{2}{\pi b^2} \left\{ e^{-\delta \hat{t}} I(\hat{t}) \sin(\omega_2 \hat{t} - \nu(\hat{t})) U(\hat{t}) \right. \\ & \left. - e^{-\delta(\hat{t} - T_0)} I(\hat{t} - T_0) \sin(\omega_2(\hat{t} - T_0) - \nu(\hat{t} - T_0)) U(\hat{t} - T_0) \right\}, \end{aligned} \quad (34)$$

where

$$I(\tau) = \sqrt{[I_1(\tau)]^2 + [I_2(\tau)]^2} \quad \text{and} \quad \nu(\tau) = \arctan\left(\frac{I_2(\tau)}{I_1(\tau)}\right). \quad (35)$$

Note that the field in the right side of Eq. (34) consists of contributions from the poles (first term) and the branch cuts (second term). The contribution from the poles has duration equal

to the incident pulse's duration, whereas the contribution from the branch cuts lasts indefinitely, albeit they exponentially dampen out. At a point $z < 0$, one does not observe the signal until the observation time t exceeds $-z/c$, which is the time it takes the signal to reach the observation point after reflection from the boundary ($z = 0$) of the dispersive medium. Then it is observed for a time T_0 , after which it rapidly diminishes to a negligible value for $t \geq T_0 + (-z/c)$. As one may deduce from the second term in Eq. (34) and the derivation preceding it, although the field diminishes exponentially as $e^{-\delta\hat{t}}$ and $e^{-\delta(\hat{t}-T_0)}$, it does not vanish identically for $t \geq T_0 + (-z/c)$. The contribution for $t \geq T_0 + (-z/c)$ arises only from the integrals along the branch cuts. If no branches were present, the reflected field would have the same duration as the incident field. Consequently, it is the presence of the branch-cut integrals that is directly responsible for broadening the time extent of the reflected field. The decay rate of the branch-cut contribution increases as the absorption coefficient δ increases, and the magnitude decreases as the square of the plasma frequency b increases.

The periodicity ($T_0 = 2n\pi/\omega_c$) of the sine function allows one to express the pole contribution in terms of the window function over $[0, T_0]$. Further note that the pole contributions result in a replica of the incident signal, which has a delay in phase as a result of the reflection from the medium's boundary and which has a magnitude that depends on the behavior of R as a function of ω_c relative to b . According to Eq. (20b), the phase delay, the argument of the reflection coefficient, is negligible when the imaginary part of $R(\omega_c)$ is nearly zero or equivalently when $\sin[(\alpha + \alpha' - \psi - \psi')/2] = 0$. On consulting the figures in the next subsection, one can deduce that this occurs in at least two situations, when $\omega_c \ll \min\{\omega_0, \delta, b\}$ or when $\omega_c \gg \max\{\omega_0, \delta, b\}$. If ω_c has the same order of magnitude as the dispersive medium's parameters, $\text{Im}[R(\omega_c)]$ cannot be approximated by zero.

Similarly, the two components of the branch-cut contributions are expressed in Eq. (34) as exponentially damped sinusoids with nonzero time-dependent phases. Although the contributions from the branch cuts are expressible individually as modulated sines, the two step functions cannot be combined to get a window function (as the pole contributions are) because $2\pi/\omega_2$ is not necessarily an integer multiple of T_0 . The first exponential term depends on \hat{t} and most affects the field just after t exceeds $-z/c$, whereas the impact of the second exponential term is not felt until t is greater than or equal to $T_0 + (-z/c)$. The preceding conclusions are illustrated by the following example.

3.1 Example of Reflected Field

In this section, the time histories of the reflected field, corresponding to eight choices of the incident field's carrier frequency ω_c at observation point $z = -10^{-5}$ m are plotted for Brillouin's choice [17] of the Lorentz medium parameters: $\omega_0 = 4.0 \times 10^{16}$ s $^{-1}$, $b^2 = 20.0 \times 10^{32}$ s $^{-2}$, and $\delta = 0.28 \times 10^{16}$ s $^{-1}$. Moreover, the incident field is taken as a single cycle of the sine function; that is, E_y^i has duration $2\pi/\omega_c$ ($n = 1$). Note that this signal is a short-pulse ultrawideband signal [18]. As Eq. (34) and the discussion following it indicate, E_y^r depends on the value of ω_c relative to the parametric frequencies ω_0 , b , and δ . In particular, the behavior of $R(\omega_c)$, as ω_c varies along the real line, is crucial to the behavior of E_y^r . Consequently, the behavior of R versus ω_c is briefly discussed before addressing E_y^r .

Figure 5 plots various aspects of $R(\omega_c)$. The horizontal axis is ω_c divided by ω_0 ; thus unity

corresponds to $\omega_c = \omega_0$. To gain additional perspective, note that $\omega_1 = 6 \times 10^{16}\text{s}^{-1}$, $\omega_2 \doteq 3.9902 \times 10^{16}\text{s}^{-1}$, $\omega_3 \doteq 5.9935 \times 10^{16}\text{s}^{-1}$, $\omega_{\pm} \doteq (\pm 3.9902 - 0.28i) \times 10^{16}\text{s}^{-1}$, and $\omega'_{\pm} \doteq (\pm 5.9935 - 0.28i) \times 10^{16}\text{s}^{-1}$, which are associated respectively with the complex numbers 1.5, 0.9975, 1.4984, $\pm 0.9975 - 0.07i$, and $\pm 1.4984 - 0.07i$ in the figures. The phase of $R(\omega_c)$ is -180° in the limit as $\omega_c \rightarrow 0+$, is strictly monotonically increasing, and asymptotically approaches 0° as ω_c increases above $2\omega_0$. In fact, for ω_c in $(0, 0.8\omega_0]$ or $[1.8\omega_0, \infty)$, $|\arg[R(\omega_c)]| \leq 10^\circ$. Consequently, the small-angle approximations to the sine and cosine of the argument of $R(\omega_c)$ are fairly accurate for this range of ω_c . The magnitude of $R(\omega_c)$ is 0.2 at $\omega_c = 0$, rises to its peak at $\omega_c \doteq 1.3\omega_0$, and falls rapidly to 0. Therefore, the magnitude of the contributions from the poles of the reflected field will be greatest for ω_c near $1.3\omega_0$. Although the pole contributions are maximized at $\omega = 1.3\omega_0$, the reflected signal with greatest energy appears at the resonance of the medium.

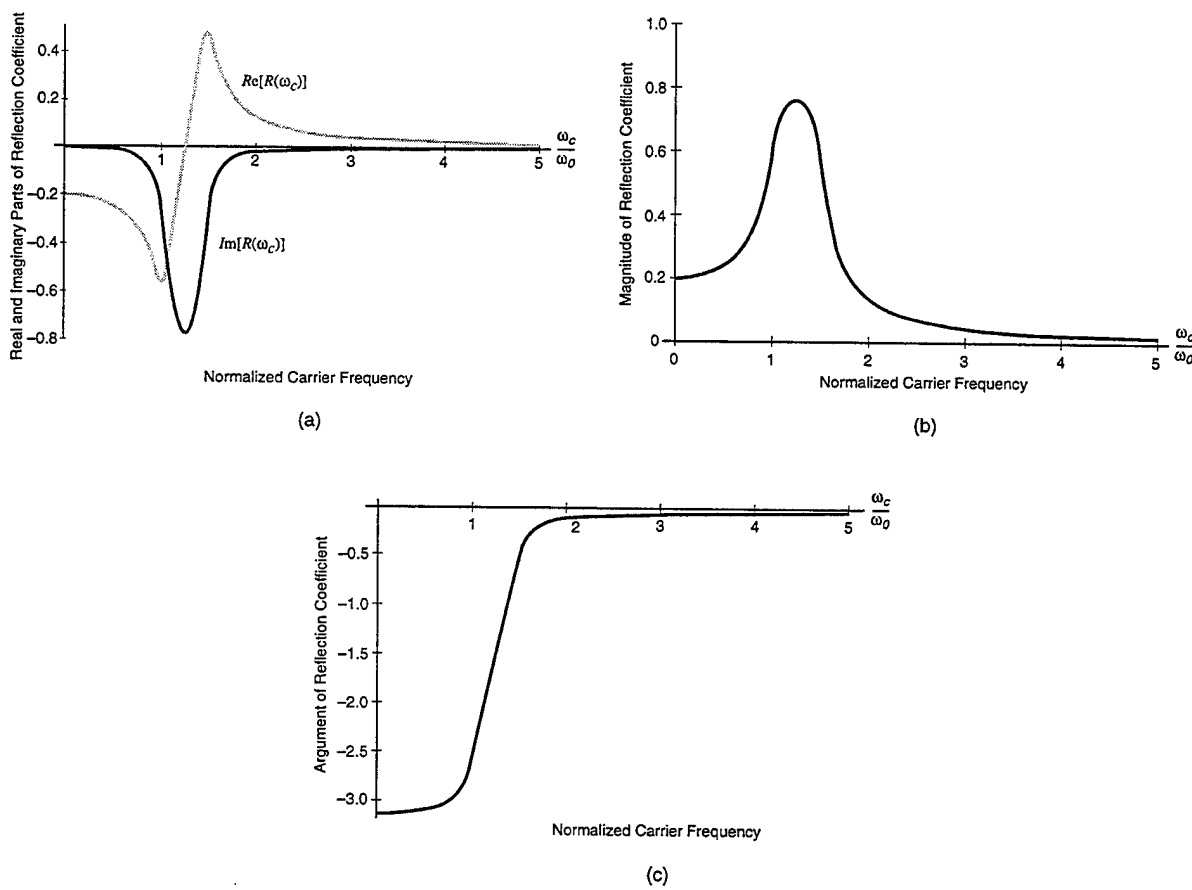


Fig. 5 – Behavior of the reflection coefficient R associated with a single-resonance Lorentz medium vs carrier frequency ω_c : (a) real (light curve) and imaginary (dark curve) parts of R , (b) magnitude of R , and (c) argument of R . The Lorentz medium is defined by $\omega_0 = 4.0 \times 10^{16}\text{s}^{-1}$, $b^2 = 20.0 \times 10^{32}\text{s}^{-2}$, and $\delta = 0.28 \times 10^{16}\text{s}^{-1}$.

To observe the distortions to the incident field that are caused by the dispersive half space, E_y^r is compared to the reflected field that is obtained when the boundary is perfectly conducting. In that case, $R(\omega)$ is identically equal to -1 , the transmitted field is zero, and the expression for the

reflected field is

$$-[U(\hat{t}) - U(\hat{t} - T_0)] \sin(\omega_c \hat{t}), \quad (36)$$

which is what one intuitively expects. Equation (36) and E_y^r are compared graphically in Fig. 6 for eight values of ω_c , where the horizontal axes are normalized time $\theta = ct/|z|$, a dimensionless quantity. Since the reflected fields are not observed until $t > |z|/c$, nonzero values do not occur until $\theta > 1$. The choices of ω_c , the associated evaluations of the reflection coefficient, and other pertinent parameters are provided in Table 2. For example, the first column of Table 2 permits one to identify ω_c with the abscissa of Fig. 6 and the value of $R(\omega_c)$. Also, since the reflected field for the perfectly conducting boundary is nonzero when $1 < \theta < 1 + cT_0/|z|^{-1}$, columns three and four give the duration and right endpoint, respectively, of this field. The smallest values ($0.0001\omega_0, 0.01\omega_0, 0.1\omega_0$) are chosen to represent the behavior of E_y^r for $\omega_c \ll \omega_0$, while $0.25\omega_0$ is chosen because it is a value that Oughstun and Sherman use in much of their work. The next largest value (ω_0) is chosen to see the impact at the dispersive medium's resonance frequency. The sixth ($1.26366\omega_0$) and seventh ($(\sqrt{13}/8)\omega_0$) values of ω_c are of interest because they are the locations of the minimum of $\text{Im}[R(\omega_c)]$ and the zero of $\text{Re}[R(\omega_c)]$, respectively. The remaining choice of ω_c is selected to represent the behavior of E_y^r for large values of the carrier frequency.

Table 2 – Choices of angular carrier frequency ω_c of the single-cycle-sine incident field for which the reflected field E_y^r is plotted in Fig. 7, as well as related evaluations.

Column 1 identifies the normalized frequency ω_c/ω_0 with ω_c ; columns 3 and 4, resp., are the normalized duration and the normalized right endpoint of the support of E_y^r when the boundary is perfectly conducting; and columns 5 and 6 are evaluations of the real and imaginary parts of the reflection coefficient R at ω_c .

ω_c/ω_0	ω_c (rad/s)	$cT_0/ z $	$1 + (cT_0/ z)$	$\text{Re}[R(\omega_c)]$	$\text{Im}[R(\omega_c)]$
0.0001	4×10^{12}	47.09129	48.09129	-0.200000	-0.000002
0.01	4×10^{14}	0.47091	1.47091	-0.200013	-0.000187
0.1	4×10^{15}	0.04709	1.04709	-0.201324	-0.001893
0.25	10^{16}	0.01884	1.01884	-0.208582	-0.005098
1	4×10^{16}	0.00471	1.00471	-0.552437	-0.276488
1.26366	5.05464×10^{16}	0.00373	1.00373	-0.032778	-0.755325
$(13/8)^{1/2}$	5.09902×10^{16}	0.00369	1.00369	0.000000	-0.754425
10	4×10^{17}	0.00047	1.00047	0.003176	-0.000045

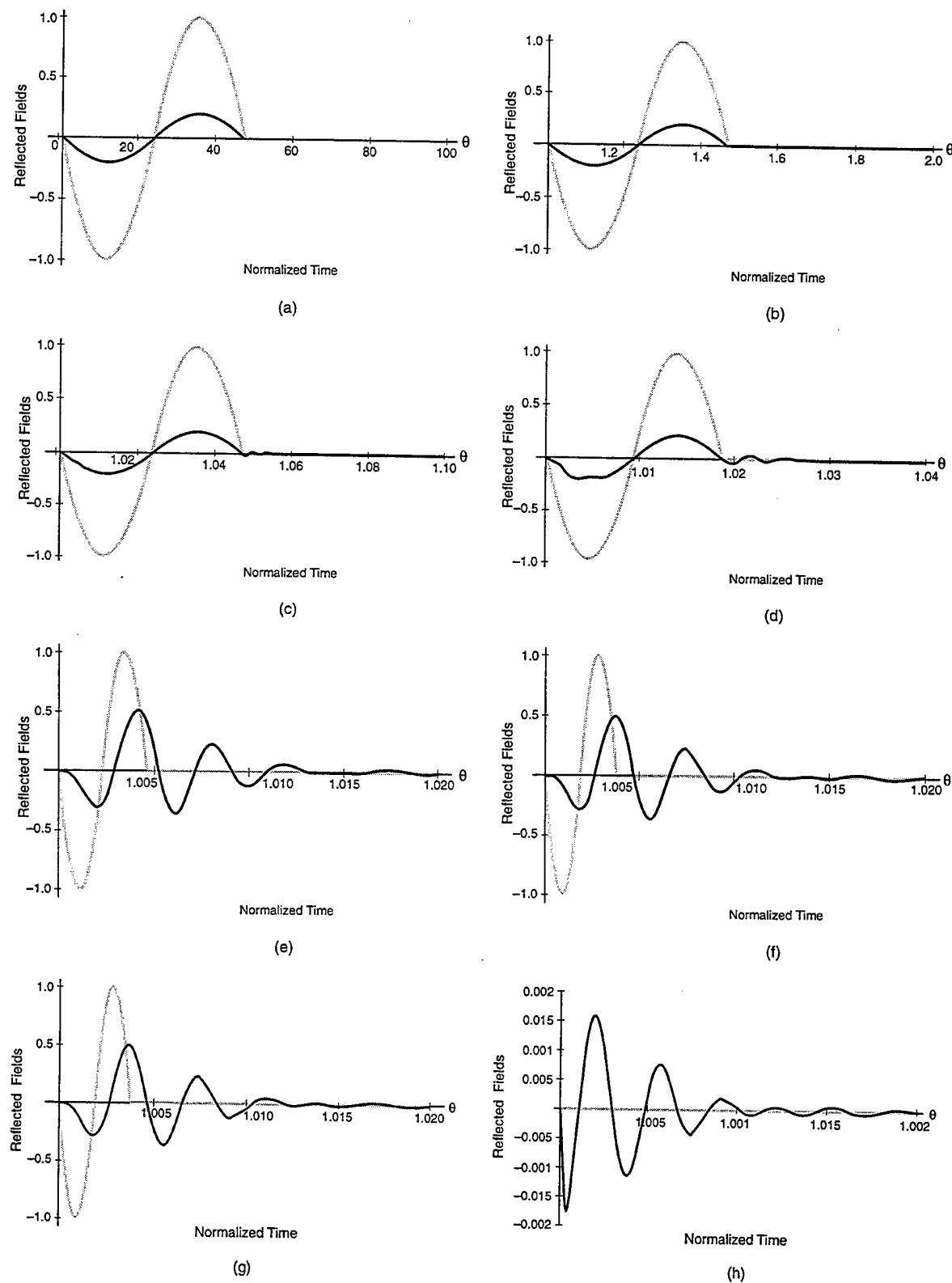


Fig. 6 – Comparison of the reflected field when the medium's boundary is perfectly conducting (light curve) and the reflected field from the Lorentz medium at $z = -10^{-5}$ m with $\omega_0 = 4.0 \times 10^{16} \text{ s}^{-1}$, $b^2 = 20.0 \times 10^{32} \text{ s}^{-2}$, and $\delta = 0.28 \times 10^{16} \text{ s}^{-1}$ (dark curve) for eight values of the carrier frequency ω_c : (a) $0.0001\omega_0$, (b) $0.01\omega_0$, (c) $0.1\omega_0$, (d) $0.25\omega_0$, (e) ω_0 , (f) $1.26366\omega_0$, (g) $\sqrt{13}/8\omega_0$, and (h) $10\omega_0$. The horizontal axes are normalized time $\theta = ct/|z|$.

After studying Fig. 6, Table 2, and Eqs. (34) and (36), one deduces several facts about the overall behavior of E_y^r as ω_c varies. Initially, for very small ω_c , E_y^r is nearly a replica of the undistorted reflected field, scaled by a factor of 0.2. Generally, as ω_c increases, the duration T_0 of the undistorted signal decreases, and the distorted field steadily broadens, so that eventually it is many times wider than the undistorted pulse. Concurrently, the maximum value of the distorted pulse increases from 0.2 to a peak of roughly 0.5 at the medium's resonance frequency ($\omega_c = \omega_0$) and then decreases to zero. As the carrier frequency increases, one also observes leading-edge distortion and damped oscillatory behavior in the field's trailing edge. Further, for very large ω_c , a steep leading edge is followed by many zero crossings.

More specifically, for very small values of ω_c ($0.0001\omega_0, 0.01\omega_0, 0.1\omega_0$), the pulse widths of E_y^r and the undistorted field are nearly the same, except for some negligible ringing in the trailing edge. As ω_c increases to $0.1\omega_0$, pulse broadening and trailing-edge ripple are more pronounced, and leading-edge distortion becomes discernible. All three effects increase as ω_c approaches the medium's resonance frequency (ω_0), where the signal attains its largest excursion (0.5) from zero. Moreover, E_y^r consists roughly of three cycles with a duration of approximately thrice the undistorted signal's pulse width. As ω_c increases above ω_0 , the pulse broadening and trailing-edge ringing are greater, but the maximum value decreases to zero. Even though $1.26366\omega_0$ and $\sqrt{13/8}\omega_0$ correspond to special values of ω_c relative to $R(\omega_c)$, the behaviors of E_y^r for these values are similar to that for ω_0 . The behavior of E_y^r for large ω_c is typified by $\omega_c = 10\omega_0$. Since the undistorted pulse for this value of the carrier has an amplitude that exceeds the peak of E_y^r by at least fifty times and occurs within the first "half cycle" of E_y^r (Table 2), the undistorted signal is not plotted.

Lastly, for $\omega_c \leq 3\omega_0$, the maximum value of E_y^r is a significant fraction (exceeds 0.2) of the amplitude of the undistorted reflected field. Clearly, a nontrivial amount of the incident field's energy resides in the reflected field for these values of ω_c . Hence, the reflected field should be included in any Lorentz formulation where the carrier frequency is less than three times the medium's resonance frequency, regardless of what portion of the electromagnetic spectrum is being considered. In particular, Oughstun's choice ($0.25\omega_0$) of ω_c falls in this range of frequencies. Moreover, because the reflected field is not negligible, it may be used as a diagnostic for the dispersive medium.

3.2 Early-Time Field Behavior

The early-time behavior of the reflected field at observation point $-z$ corresponds to t slightly greater than $-z/c$. Consequently, the reflected field is analyzed for $-z/c \leq t \leq -z/c + t_e$ ($0 \leq \hat{t} \leq t_e$), where t_e is a small positive number less than T_0 . Hence in Eq. (34), $U(\hat{t} - T_0) = 0$ for $0 \leq \hat{t} \leq t_e$, and the early-time reflected field is

$$E_{y,et}^r(z, t) = \left[\sin(\omega_c \hat{t}) \operatorname{Re}[R(\omega_c)] - \cos(\omega_c \hat{t}) \operatorname{Im}[R(\omega_c)] \right] + \frac{2}{\pi b^2} e^{-\delta \hat{t}} \left[\sin(\omega_2 \hat{t}) \mathcal{I}_1(\hat{t}) - \cos(\omega_2 \hat{t}) \mathcal{I}_2(\hat{t}) \right]. \quad (37)$$

Alternatively, when closed-form solutions are unavailable, one resorts to high-frequency approximations of various quantities to obtain analytical expressions. The remainder of the subsection is spent on deriving a high-frequency representation of E_y^r . Begin with Eq. (16) and recast it as

$$E_y^r(z, t) = \int_{-\infty+ia}^{\infty+ia} Q(\omega) R(\omega) \tilde{A}(\omega - \omega_c) e^{-i\omega \hat{t}} d\omega - \int_{-\infty+ia}^{\infty+ia} Q(\omega) R(\omega) \tilde{A}(\omega + \omega_c) e^{-i\omega \hat{t}} d\omega, \quad (38)$$

where

$$Q(\omega) = \frac{1}{4\pi} (e^{i\omega T_0} - 1) \quad \text{and} \quad \tilde{A}(\omega) = \frac{1}{\omega}. \quad (39)$$

Because $[n(\omega^*)]^* = n(-\omega)$, it follows from Eqs. (10b) and (39) that $R^*(\omega^*) = R(-\omega)$, $\tilde{A}(-\omega^* - \omega_c) = -\tilde{A}^*(\omega - \omega_c)$, and $Q^*(\omega^*) = Q(-\omega)$. In the second integral of Eq. (38), make the change of variable $\eta = \omega^*$ and apply the preceding properties to get

$$E_y^r(z, t) = \operatorname{Re} \left[\int_{-\infty+ia}^{\infty+ia} \frac{R(\omega)}{2\pi(\omega - \omega_c)} e^{-i\omega(t-T)} d\omega - \int_{-\infty+ia}^{\infty+ia} \frac{R(\omega)}{2\pi(\omega - \omega_c)} e^{-i\omega t} d\omega \right]. \quad (40)$$

The reflected field is now ready for approximate analysis. The Laurent series,

$$\begin{aligned} n(\omega) &= \left[1 - \frac{b^2}{2} \left(\frac{\varphi_1}{\omega^2} + \frac{\varphi_2}{\omega^4} + \frac{\varphi_3}{\omega^6} \right) + R_{n1}(\omega^{-8}) \right] \\ &\quad + i \left[\frac{b^2}{2} \left(\frac{2\psi_1}{\omega^3} + \frac{2\psi_2}{\omega^5} + \frac{2\psi_3}{\omega^7} \right) + R_{n2}(\omega^{-9}) \right], \end{aligned} \quad (41)$$

$$\begin{aligned} \frac{R(\omega)}{\omega - \omega_c} &= \frac{b^2}{4} \left[\frac{a_2}{\omega^3} + \frac{a_2\omega_c}{\omega^4} + \frac{a_4 + a_2\omega_c^2}{\omega^5} + \frac{\omega_c(a_4 + a_2\omega_c^2)}{\omega^6} + R_{F1}(\omega^{-7}) \right] \\ &\quad - i \frac{b^2}{4} \left[\frac{a_3}{\omega^4} + \frac{a_3\omega_c}{\omega^5} + \frac{a_5 + a_3\omega_c^2}{\omega^6} + \frac{\omega_c(a_5 + a_3\omega_c^2)}{\omega^7} + R_{F2}(\omega^{-8}) \right], \end{aligned} \quad (42)$$

are obtained after several applications of the binomial series for large ω , where

$$\begin{aligned} \varphi_1 &= 1, \\ \varphi_2 &= \omega_0^2 - 4\delta^2 + \frac{1}{4}b^2, \\ \varphi_3 &= \omega_0^4 - 12\delta^2\omega_0^2 + \frac{1}{2}b^2\omega_0^2 - 3b^2\delta^2 + \frac{1}{8}b^4 + 16\delta^4, \\ \psi_1 &= \delta, \\ \psi_2 &= 2\delta \left(\omega_0^2 - 2\delta^2 + \frac{1}{4}b^2 \right), \\ \psi_3 &= \frac{\delta}{2} \left(6\omega_0^4 - 32\delta^2\omega_0^2 + 3b^2\omega_0^2 + \frac{5}{2}b^4 \right), \\ a_2 &= \varphi_1, \\ a_3 &= 2\psi_1, \\ a_4 &= \varphi_2 + \frac{b^2}{4}\varphi_1^2, \\ a_5 &= 2\psi_2 + b^2\varphi_1\psi_1, \\ a_6 &= \varphi_3 + \frac{b^2}{4} \left(2\varphi_1\varphi_2 + \frac{b^2}{4}\varphi_1^3 - 4\psi_1^2 \right), \\ a_7 &= 2\psi_3 + b^2 \left(\varphi_1\psi_2 + \psi_1\varphi_2 + \frac{3b^2}{8}\psi_1\varphi_1^2 \right). \end{aligned} \quad (43)$$

The functions R_{n1} , R_{n2} , R_{F1} , and R_{F2} represent the remainders of series, and their arguments indicate the lowest-order terms in the remainders. The high-frequency representation for $n(\omega)$, as

a Laurent series, effectively eliminates the branch points as singularities. As will be seen shortly, this greatly simplifies evaluation of the integrals in Eq. (40).

Since each integral in Eq. (40) has the same general form, consider

$$\int_{-\infty+ia}^{\infty+ia} \frac{R(\omega)}{2\pi(\omega - \omega_c)} e^{-i\omega\tau} d\omega.$$

Recall from the discussion regarding Eq. (18) that C_1 is the finite version of the path C in the preceding integral. By closing C_1 with a semicircle of radius F from above and by letting $F \rightarrow \infty$, the path integral is zero for $\tau \leq 0$. For positive τ , the Jordan contour is simply $C_1 + C_{FL}$, where C_{FL} is the semicircle of radius F that connects the ends of C_1 from below (Fig. 7). According to the Cauchy Integral Formula,¹⁹

$$\lim_{F \rightarrow +\infty} \int_{C_1 + C_{FL}} \frac{e^{-i\omega\tau}}{\omega^{n+1}} d\omega = \frac{2\pi}{n!} (-i)^{n+1} \tau^n.$$

Substituting the high-frequency representation of $R(\omega)(\omega - \omega_c)^{-1}$ given by Eq. (42), integrating term by term, and applying the Cauchy Integral Formulas yield

$$\int_{-\infty+ia}^{\infty+ia} \frac{R(\omega)}{2\pi(\omega - \omega_c)} e^{-i\omega\tau} d\omega = U(\tau) \frac{b^2}{4} \left\{ \left[\frac{a_2 \omega_c}{3!} \tau^3 - \frac{a_3 \omega_c}{4!} \tau^4 - \frac{\omega_c (a_4 + a_2 \omega_c^2)}{5!} \tau^5 + \frac{\omega_c (a_5 + a_3 \omega_c^2)}{6!} \tau^6 \right. \right. \\ \left. \left. + R_1(\tau^7) \right] + i \left[\frac{a_2}{2!} \tau^2 - \frac{a_3}{3!} \tau^3 - \frac{a_4 + a_2 \omega_c^2}{4!} \tau^4 + \frac{a_5 + a_3 \omega_c^2}{5!} \tau^5 + R_2(\tau^6) \right] \right\}, \quad (44)$$

where R_1 and R_2 are the series' remainders for the real and imaginary parts, respectively.

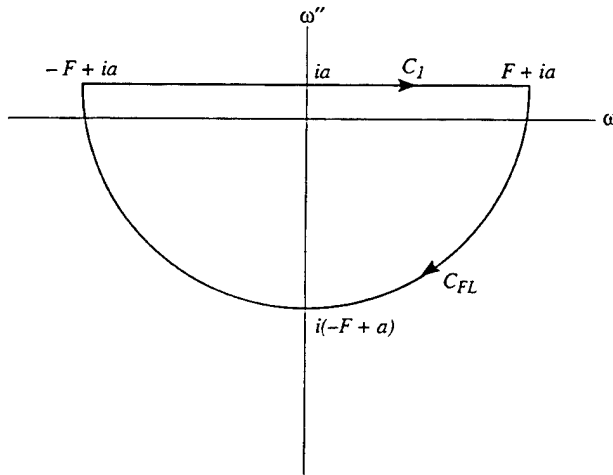


Fig. 7 – Closed Jordan contour $C_1 + C_{FL}$, oriented in the clockwise direction, consists of the line segment C_1 and the semicircle C_{FL} . The line segment goes from $-F + ia$ to $F + ia$, and the semicircle has radius F and center at $\omega = ia$.

Setting τ equal to $\hat{t} - T_0$ and \hat{t} in Eq. (44), substituting those expressions into Eq. (40), and using Eqs. (43) lead to

$$\begin{aligned} E_{y,hf}^r(z, t) = & U(\hat{t} - T_0) \frac{b^2}{4} \left[\frac{\omega_c}{3!} (\hat{t} - T_0)^3 - \frac{2\delta\omega_c}{4!} (\hat{t} - T_0)^4 - \frac{\omega_c}{5!} \left(\omega_0^2 - 4\delta^2 + \frac{b^2}{2} + \omega_c^2 \right) (\hat{t} - T_0)^5 \right. \\ & + \frac{2\delta\omega_c}{6!} (2\omega_0^2 - 4\delta^2 + b^2 + \omega_c^2) (\hat{t} - T_0)^6 + R_1((\hat{t} - T_0)^7) \left. \right] \\ & - U(\hat{t}) \frac{b^2}{4} \left[\frac{\omega_c}{3!} \hat{t}^3 - \frac{2\delta\omega_c}{4!} \hat{t}^4 - \frac{\omega_c}{5!} \left(\omega_0^2 - 4\delta^2 + \frac{b^2}{2} + \omega_c^2 \right) \hat{t}^5 \right. \\ & + \frac{2\delta\omega_c}{6!} (2\omega_0^2 - 4\delta^2 + b^2 + \omega_c^2) \hat{t}^6 + R_1(\hat{t}^7) \left. \right], \end{aligned} \quad (45)$$

a high-frequency representation of E_y^r . This result is obtained by assuming that $|\omega|$ is large enough to ensure the convergence of the series used to obtain $R(\omega)(\omega - \omega_c)^{-1}$. At the very least, $|\omega| > \max\{\omega_c, \omega_0, \delta, b\}$. Moreover, when $|\omega|$ is large enough, $0 \leq \hat{t} \leq t_\epsilon$ and $U(\hat{t} - T_0) \equiv 0$. Thus for $0 \leq \hat{t} \leq t_\epsilon$,

$$\begin{aligned} E_{y,hf}^r(z, t) = & -\frac{b^2}{4} \left[\frac{\omega_c}{3!} \hat{t}^3 - \frac{2\delta\omega_c}{4!} \hat{t}^4 - \frac{\omega_c}{5!} \left(\omega_0^2 - 4\delta^2 + \frac{b^2}{2} + \omega_c^2 \right) \hat{t}^5 \right. \\ & + \frac{2\delta\omega_c}{6!} (2\omega_0^2 - 4\delta^2 + b^2 + \omega_c^2) \hat{t}^6 + R_1(\hat{t}^7) \left. \right]. \end{aligned} \quad (46)$$

In the limit as the attenuation factor δ goes to zero, Eq. (46) reduces to

$$E_{y,hf}^r(z, t) = \frac{b^2}{4} \left[-\frac{\omega_c}{3!} \hat{t}^3 + \frac{\omega_c}{5!} \left(\omega_0^2 + \frac{b^2}{2} + \omega_c^2 \right) \hat{t}^5 + R_1(\hat{t}^7) \right], \quad (47)$$

which is Colby's result when his parameter θ is evaluated at zero.²⁰

To compare Eqs. (37) and (46), Brillouin's choice of parameters for a Lorentz medium are used ($\omega_0 = 4.0 \times 10^{16} \text{ s}^{-1}$, $b^2 = 20.0 \times 10^{32} \text{ s}^{-2}$, $\delta = 0.28 \times 10^{16} \text{ s}^{-1}$), and the frequency ω_c of the incident field is 10^{16} s^{-1} . As Fig. 8 illustrates, at an observation point that is 10^{-5} meters to the left of the dispersive medium's boundary, $E_{y,et}^r$ (lower curve) and $E_{y,hf}^r$ (upper curve) agree extremely well for $1 \leq \theta \leq 1.0013$. Both signals are not observed until 33.36 femtoseconds (fs) after the incident field encounters the medium. For the first 43.36 attoseconds (as) after their initial observation, they are visually indistinguishable. At that point, they start separating rapidly because the high-frequency approximation is no longer valid.

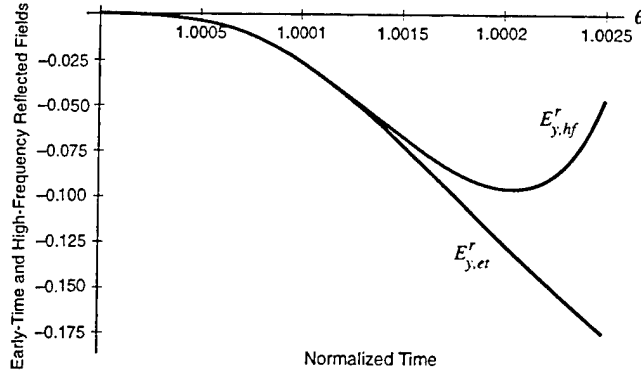


Fig. 8 – Early-time (lower curve) and high-frequency (upper curve) fields vs normalized time $\theta = ct/|z|$ at $z = -10^{-5}$ m for $\omega_0 = 4.0 \times 10^{16}$ s $^{-1}$, $b^2 = 20.0 \times 10^{32}$ s $^{-2}$, and $\delta = 0.28 \times 10^{16}$ s $^{-1}$.

4. EVALUATION OF TRANSMITTED FIELD

Since a closed-form evaluation of the inversion integral in Eq. (11(b)) is unlikely, one must resort either to numerical evaluation of the inversion integral or to an asymptotic approximation of it. In this report, the latter approach is taken for observation points that are sufficiently far from the dispersive medium's boundary to ensure the validity of asymptotically representing the fields. The inversion integral, a Generalized Laplace Integral [21,22], is treated with existing uniform asymptotic methods. Detailed discussions of uniform asymptotic techniques are found in Refs. 23–27.

Details of the methodology for obtaining a uniform asymptotic expansion of the transmitted field for a constant (unity) transmission coefficient are found in Refs. 4 and 6–8. The purpose of this section is to show how inclusion of a frequency-dependent transmission coefficient impacts the transmitted field.

4.1 Inclusion of Transmission Coefficient in Transmitted Field

In the notation of Oughstun, Eq. (11(b)) becomes

$$E_y^t(z, t) = \mathcal{E}_y^t(z, \theta) = \int_{-\infty+ia}^{\infty+ia} A(\omega) T(\omega) e^{\frac{z}{c} \phi(\omega, \theta)} d\omega, \quad (48)$$

where the dimensionless parameter $\theta = ct/z$ can be viewed as normalized time and

$$\phi(\omega, \theta) = i\omega[n(\omega) - \theta]. \quad (49)$$

The symbols \mathcal{E} and A are used for the fields when they depend on θ instead of time t . Although the right side of Eq. (48) is similar to the equations given in Ref. 28, it differs in two ways: (1) the missing factor of 2π , which comes from the difference in the definitions of the Fourier transform,

and (2) the inclusion of the transmission coefficient $T(\omega)$. The saddle points of Eq. (48) are the critical points of the generalized phase ϕ , which are the roots of

$$n(\omega) + \omega n'(\omega) - \theta = 0. \quad (50)$$

When $\theta < 1$ ($t < z/c$), one can show that $\mathcal{E}_y^t(E_y^t) = 0$ by closing C_1 with a semicircle from above. Thus at a fixed observation point z within the dispersive medium, no signal is observed until the leading edge of the incident field traverses the distance z . When $\theta \geq 1$, it is well-known that the inversion integral can be evaluated by closing C_1 so that the resulting Jordan contour $C_J(\theta)$ passes through the saddle points via the subcontour $P(\theta) = P_N(\theta) + P_D(\theta)$ [29,30] and so that the integrals over subcontours other than C and $P(\theta)$ go to zero via some limiting process.

To evaluate the integral representation of E_y^t , first observe that the Fourier transform \hat{M} of an arbitrary modulation function M is related to A (Eq. (10(a))) by

$$A(\omega) = -\frac{i}{2} [\hat{M}(\omega + \omega_c) - \hat{M}(\omega - \omega_c)]. \quad (51)$$

The difference between the \tilde{u} of Oughstun and Sherman and \hat{M} arises from the 2π variance in the definitions of the Fourier transform; that is, $2\pi\hat{M} = \tilde{u}$. Substituting Eq. (51) into Eq. (48) yields

$$\mathcal{E}_y^t(z, \theta) = \frac{-i}{2} \left[\int_{-\infty+ia}^{\infty+ia} T(\omega) \hat{M}(\omega + \omega_c) e^{\frac{z}{c}\phi(\omega, \theta)} d\omega - \int_{-\infty+ia}^{\infty+ia} T(\omega) \hat{M}(\omega - \omega_c) e^{\frac{z}{c}\phi(\omega, \theta)} d\omega \right]. \quad (52)$$

Because M is zero for $t < 0$ and is real-valued for $t \geq 0$, \hat{M} satisfies $\hat{M}(-\omega) = [\hat{M}(\omega^*)]^*$. Consequently, $\phi^*(\omega^*, \theta) = \phi(-\omega, \theta)$, $T^*(\omega^*) = T(-\omega)$, and $\hat{M}(-(\omega - \omega_c)^*) = [\hat{M}(\omega - \omega_c)]^*$, which imply that the first integral in Eq. (52) is the complex conjugate of the second integral. Hence,

$$\mathcal{E}_y^t(z, \theta) = \text{Re} \left[\frac{i}{2\pi} \int_{-\infty+ia}^{\infty+ia} T(\omega) \tilde{u}(\omega - \omega_c) e^{\frac{z}{c}\phi(\omega, \theta)} d\omega \right], \quad (53)$$

which is Eq. (1.11) of Ref. 7 and Eq. (7.2.1) of Ref. 8 with $T(\omega) \equiv 1$.

To this point, the results are general. When M is the window function defined by Eq. (12),

$$\tilde{u}(\omega) = \frac{e^{i\omega T_0} - 1}{i\omega} \quad (54)$$

and

$$\mathcal{E}_y^t(z, \theta) = \mathcal{A}(z, \theta, 0) - \mathcal{A}(z, \theta, T_0), \quad (55)$$

where

$$\theta_{T_0} = \theta - \frac{cT_0}{z} \quad \text{and} \quad \mathcal{A}(z, \theta, T_0) = -\frac{1}{2\pi} \text{Re} \left[e^{-i\omega_c T_0} \int_{-\infty+ia}^{\infty+ia} \frac{T(\omega)}{\omega - \omega_c} e^{\frac{z}{c}\phi(\omega, \theta_{T_0})} d\omega \right]. \quad (56)$$

To determine the transmitted field, one need only derive $\mathcal{A}(z, \theta, T_0)$ and take the limit as T_0 approaches zero to obtain $\mathcal{A}(z, \theta, 0)$. For $\mathcal{A}(z, \theta, T_0)$, apply Cauchy's residue theorem to obtain the

decomposition of Oughstun and Sherman,

$$\begin{aligned}
 \mathcal{A}(z, \theta, T_0) &= -\frac{U(\theta T_0)}{2\pi} \operatorname{Re} \left[e^{-i\omega_c T_0} \int_{P_D(\theta)} \frac{T(\omega)}{\omega - \omega_c} e^{\frac{z}{c}\phi(\omega, \theta T_0)} d\omega \right] \\
 &\quad - \frac{U(\theta T_0)}{2\pi} \operatorname{Re} \left[e^{-i\omega_c T_0} \int_{P_N(\theta)} \frac{T(\omega)}{\omega - \omega_c} e^{\frac{z}{c}\phi(\omega, \theta T_0)} d\omega \right] \\
 &\quad - \frac{U(\theta T_0)}{2\pi} \operatorname{Re} \left[-2\pi i e^{-i\omega_c T_0} \sum \text{Residues enclosed by } C_J(\theta) \right] \\
 &= \mathcal{A}_S(z, \theta, T_0) + \mathcal{A}_B(z, \theta, T_0) + \mathcal{A}_C(z, \theta, T_0), \tag{57}
 \end{aligned}$$

where the first, second, and third terms following the first equal sign correspond to \mathcal{A}_S , \mathcal{A}_B , and \mathcal{A}_C , respectively.

Note that $\mathcal{A}(z, \theta, T_0)$ and $\mathcal{A}(z, \theta, 0)$ are zero for $\theta \leq 1$ and $\theta \leq cT_0/z$, respectively, and that each is basically the integral along $P(\theta)$ plus contributions from poles of the transmission coefficient T and the Fourier-transformed modulation function M that lie inside $C_J(\theta)$. The Generalized Laplace Integrals in Eq. (57) are evaluated with uniform asymptotic expansions relative to the secondary parameter θ as z increases without bound [23,25,26].

The methodology of Oughstun and Sherman [31], which combines uniform asymptotic results from five sources [27,32–35], is followed to get a uniform asymptotic representation of \mathcal{E}_y^t . Defining $\mathcal{A}_j(z, \theta) = \mathcal{A}_j(z, \theta, 0) - \mathcal{A}_j(z, \theta, T_0)$ for j in $\{S, B, C\}$ implies

$$\mathcal{E}_y^t(z, \theta) = \mathcal{A}_S(z, \theta) + \mathcal{A}_B(z, \theta) + \mathcal{A}_C(z, \theta). \tag{58}$$

The contributions \mathcal{A}_S (Sommerfeld's precursor field), \mathcal{A}_B (Brillouin's precursor field), and \mathcal{A}_C (main signal) depend respectively on the behavior of the distant saddle points, on the behavior of the near saddle points, and on the location of the poles of $T(\omega)\hat{M}(\omega - \omega_c)$ relative to path $P(\theta)$. Since the refractive index is bounded away from -1 , T has no poles and is bounded. Hence, the pole contributions come solely from \hat{M} , whose only pole is located at ω_c .

4.2 Saddle Points of ϕ

As mentioned earlier, the saddle points of Eq. (48) are the roots of Eq. (50). After substituting Eq. (6) into Eq. (50), eliminating the square root, and manipulating the resulting equation, one obtains the following eighth-degree polynomial in ω ,

$$\begin{aligned}
 0 &= [\theta^2 - 1]\omega^8 + [8\delta i(\theta^2 - 1)]\omega^7 - [4(6\delta^2 + \omega_0^2)(\theta^2 - 1) + b^2\theta^2]\omega^6 \\
 &\quad - [2\delta i((12\omega_0^2 + 3b^2 + 16\delta^2)(\theta^2 - 1) + 2b^2)]\omega^5 \\
 &\quad + [(6\omega_0^4 + 48\delta^2\omega_0^2 + 2b^2\omega_0^2 + 12b^2\delta^2 + 16\delta^4)(\theta^2 - 1) + b^2(\omega_0^2\theta^2 - 12\delta^2) + 16b^2\delta^2]\omega^4 \\
 &\quad + [4\delta i((6\omega_0^4 + 3b^2\omega_0^2 + 8\delta^2\omega_0^2 + 2b^2\delta^2)(\theta^2 - 1) - b^2(2\omega_0^2 + 3\delta^2) + b^2(2\omega_0^2 + 3\delta^2))]\omega^3 \\
 &\quad - [\omega_0^2(4\omega_0^4 + 3b^2\omega_0^2 + 24\delta^2\omega_0^2 + 12b^2\delta^2)(\theta^2 - 1) \\
 &\quad \quad - b^2(\omega_0^4 + 20\delta^2\omega_0^2 + 9b^2\delta^2) + 8b^2\delta^2(2\omega_0^2 + b^2)]\omega^2 \\
 &\quad - [2\delta i\omega_0^2((4\omega_0^2 + 3b^2)(\omega_0^2(\theta^2 - 1) - b^2) + 2b^2(\omega_0^2 + b^2))]\omega \\
 &\quad + [\omega_0^4(\omega_0^2 + b^2)(\omega_0^2(\theta^2 - 1) - b^2)], \tag{59}
 \end{aligned}$$

that must be solved to obtain the saddle points. It turns out that Eq. (50) has exactly four saddle points. Consequently, the squaring operation that leads to Eq. (59) introduces four extraneous roots. The saddle points are symmetric with respect to the imaginary axis in the complex ω plane and fall naturally into two categories, those that are near the origin (ω_{N1} and ω_{N2}) and those that are far from the origin (ω_{D1} and ω_{D2}).

To place the following brief discussion in context, a few of the salient features of the dynamical behavior (θ dependence) of the saddle points [36] are first summarized. The near saddle points lie along the imaginary axis for $\theta = 1$, with ω_{N1} being the upper one. As θ increases, they approach each other on the imaginary axis until they coalesce to a second-order saddle point at θ_1 . As θ continues to increase beyond θ_1 , the near saddle points symmetrically separate with increasing distance between them. In the limit as $\theta \rightarrow \infty$, they approach the branch points ω_{\pm} . On the other hand, the distant saddle points always lie in the lower half of the complex plane. Moreover, they are located at $\pm\infty - 2\delta i$ when $\theta = 1$ and move towards the branch cut as θ increases, with $\lim_{\theta \rightarrow \infty} \omega_{D1} = \omega'_+$ and $\lim_{\theta \rightarrow \infty} \omega_{D2} = \omega'_-$.

On comparing Eq. (59) with Eq. (4.2.5) in Ref. 4 and Eq. (6.2.5) in Ref. 8, one observes discrepancies in the coefficients of $\omega^1, \omega^2, \omega^3, \omega^4$, and ω^5 . To ascertain the impact of the difference between the two polynomials, the saddle points of both polynomials are calculated for Brillouin's choice of Lorentz parameters ($\omega_0 = 4.0 \times 10^{16}/s$, $b^2 = 20.0 \times 10^{32}/s^2$, $\delta = 0.28 \times 10^{16}/s$). These values, computed independently with *Mathematica* and *MATLAB*, are provided in Tables 3 and 4. Although the roots are computed to 12 decimal places, the tabulated entries are rounded to 3 decimal places to conserve space. The values of θ at which the roots are determined are chosen so that the computed values may be compared with values that are visually estimated from Figs. 6.15, 6.16, and 6.17 of Ref. 8.

Table 3 – Distant saddle points ω_{D1} , roots from two distinct eighth-degree polynomials, vs normalized time θ . Column 2 is calculated with Eq. (66). Column 3 is calculated with Eq. (6.2.5) of Oughstun and Sherman.^a

θ	$\omega_{D1} \cdot 10^{-16}$ (rad/s)	$\omega_{D1} \cdot 10^{-16}$ (rad/s)
1.000	$\infty - 0.560i$	$\infty - 1.120i$
1.009	$34.245 - 0.541i$	$34.264 - 1.062i$
1.010	$32.580 - 0.539i$	$32.600 - 1.056i$
1.015	$26.971 - 0.530i$	$26.993 - 1.029i$
1.020	$23.667 - 0.522i$	$23.690 - 1.005i$
1.025	$21.437 - 0.515i$	$21.460 - 0.983i$
1.030	$19.807 - 0.508i$	$19.830 - 0.962i$
1.040	$17.548 - 0.496i$	$17.571 - 0.926i$
1.050	$16.032 - 0.486i$	$16.054 - 0.895i$
1.100	$12.389 - 0.449i$	$12.406 - 0.787i$
1.150	$10.849 - 0.427i$	$10.863 - 0.719i$
1.200	$9.960 - 0.411i$	$9.971 - 0.672i$
1.250	$9.369 - 0.399i$	$9.378 - 0.636i$
1.300	$8.940 - 0.389i$	$8.948 - 0.608i$
1.400	$8.353 - 0.375i$	$8.359 - 0.565i$
1.500	$7.964 - 0.365i$	$7.968 - 0.534i$
1.502735905	$7.955 - 0.364i$	$7.959 - 0.533i$
1.510	$7.932 - 0.364i$	$7.936 - 0.531i$
1.520	$7.901 - 0.363i$	$7.905 - 0.529i$
1.530	$7.871 - 0.362i$	$7.874 - 0.526i$
1.540	$7.842 - 0.361i$	$7.845 - 0.524i$
1.550	$7.814 - 0.360i$	$7.817 - 0.521i$
1.600	$7.684 - 0.356i$	$7.686 - 0.510i$
1.700	$7.471 - 0.350i$	$7.473 - 0.490i$
1.800	$7.303 - 0.345i$	$7.304 - 0.474i$
1.900	$7.166 - 0.340i$	$7.167 - 0.460i$
2.000	$7.053 - 0.336i$	$7.053 - 0.448i$
2.500	$6.690 - 0.322i$	$6.688 - 0.405i$
3.000	$6.493 - 0.313i$	$6.491 - 0.378i$
4.000	$6.290 - 0.302i$	$6.287 - 0.346i$
5.000	$6.190 - 0.295i$	$6.187 - 0.327i$
10.000	$6.046 - 0.285i$	$6.045 - 0.294i$
20.000	$6.007 - 0.281i$	$6.007 - 0.284i$
100.000	$5.994 - 0.280i$	$5.994 - 0.280i$
1000.000	$5.993 - 0.280i$	$5.994 - 0.280i$
∞	$5.993 - 0.280i$	$5.993 - 0.280i$

^aK.E. Oughstun and G.C. Sherman, Electromagnetic Pulse Propagation in Causal Dielectrics (Springer-Verlag, Berlin, 1994), Ch. 6, p. 208.

Table 4 – Near saddle points $\{\omega_{N1}, \omega_{N2}\}$, roots from two distinct eighth-degree polynomials, versus normalized time θ . Columns 2 and 4 are calculated with Eq. (66). Columns 3 and 5 are calculated with Eq. (6.2.5) of Oughstun and Sherman.^a

θ	$\omega_{N1} \cdot 10^{-16}$ (rad/s)	$\omega_{N1} \cdot 10^{-16}$ (rad/s)	$\omega_{N2} \cdot 10^{-16}$ (rad/s)	$\omega_{N2} \cdot 10^{-16}$ (rad/s)
1.000	$4.474 i$	$5.080 i$	$-4.461 i$	$-3.924 i$
1.009	$4.297 i$	$4.854 i$	$-4.322 i$	$-3.814 i$
1.010	$4.278 i$	$4.831 i$	$-4.307 i$	$-3.802 i$
1.015	$4.189 i$	$4.720 i$	$-4.236 i$	$-3.745 i$
1.020	$4.105 i$	$4.616 i$	$-4.168 i$	$-3.690 i$
1.025	$4.024 i$	$4.518 i$	$-4.102 i$	$-3.636 i$
1.030	$3.948 i$	$4.426 i$	$-4.039 i$	$-3.584 i$
1.040	$3.805 i$	$4.255 i$	$-3.920 i$	$-3.485 i$
1.050	$3.673 i$	$4.100 i$	$-3.809 i$	$-3.391 i$
1.100	$3.127 i$	$3.474 i$	$-3.335 i$	$-2.981 i$
1.150	$2.695 i$	$2.995 i$	$-2.948 i$	$-2.635 i$
1.200	$2.326 i$	$2.592 i$	$-2.610 i$	$-2.326 i$
1.250	$1.992 i$	$2.234 i$	$-2.300 i$	$-2.038 i$
1.300	$1.677 i$	$1.900 i$	$-2.003 i$	$-1.758 i$
1.400	$1.040 i$	$1.230 i$	$-1.393 i$	$-1.171 i$
1.500	$0.000 i$	$0.000 - 0.000 i$	$-0.373 i$	$-0.000 i$
1.503 ^b	$0.000 - 0.187 i$	$0.186 - 0.001 i$	$0.000 - 0.187 i$	$0.186 - 0.001 i$
1.510	$0.302 - 0.187 i$	$0.355 - 0.003 i$	$0.302 + 0.187 i$	$0.355 + 0.003 i$
1.520	$0.463 - 0.188 i$	$0.499 - 0.005 i$	$0.463 + 0.188 i$	$0.499 + 0.005 i$
1.530	$0.579 - 0.189 i$	$0.608 - 0.007 i$	$0.579 + 0.189 i$	$0.608 + 0.007 i$
1.540	$0.673 - 0.190 i$	$0.698 - 0.010 i$	$0.673 + 0.190 i$	$0.698 + 0.010 i$
1.550	$0.754 - 0.191 i$	$0.776 - 0.012 i$	$0.754 + 0.191 i$	$0.776 + 0.012 i$
1.600	$1.054 - 0.194 i$	$1.069 - 0.023 i$	$1.054 + 0.194 i$	$1.069 + 0.023 i$
1.700	$1.432 - 0.200 i$	$1.442 - 0.041 i$	$1.432 + 0.200 i$	$1.442 + 0.041 i$
1.800	$1.685 - 0.205 i$	$1.693 - 0.056 i$	$1.685 + 0.205 i$	$1.693 + 0.056 i$
1.900	$1.875 - 0.209 i$	$1.882 - 0.068 i$	$1.875 + 0.209 i$	$1.882 + 0.068 i$
2.000	$2.026 - 0.213 i$	$2.031 - 0.079 i$	$2.026 + 0.213 i$	$2.031 + 0.079 i$
2.500	$2.490 - 0.225 i$	$2.493 - 0.116 i$	$2.490 + 0.225 i$	$2.493 + 0.116 i$
3.000	$2.742 - 0.233 i$	$2.745 - 0.139 i$	$2.742 + 0.233 i$	$2.745 + 0.139 i$
4.000	$3.025 - 0.242 i$	$3.027 - 0.166 i$	$3.025 + 0.242 i$	$3.027 + 0.166 i$
5.000	$3.186 - 0.248 i$	$3.187 - 0.183 i$	$3.186 + 0.248 i$	$3.187 + 0.183 i$
10.000	$3.510 - 0.260 i$	$3.511 - 0.219 i$	$3.510 + 0.260 i$	$3.511 + 0.219 i$
20.000	$3.694 - 0.267 i$	$3.695 - 0.241 i$	$3.694 + 0.267 i$	$3.695 + 0.241 i$
100.000	$3.890 - 0.275 i$	$3.890 - 0.266 i$	$3.890 + 0.275 i$	$3.890 + 0.266 i$
1000.000	$3.969 - 0.279 i$	$3.969 - 0.277 i$	$3.969 + 0.279 i$	$3.969 + 0.277 i$
∞	$3.990 - 0.280 i$	$3.990 - 0.280 i$	$3.990 + 0.280 i$	$3.990 + 0.280 i$

^aK.E. Oughstun and G.C. Sherman, *Electromagnetic Pulse Propagation in Causal Dielectrics* (Springer-Verlag, Berlin, 1994), Ch. 6, p. 208.

^b1.502735905 is rounded to conserve space.

The values calculated with Eq. (49) (column 2 of Table 3, columns 2 and 4 of Table 4) do not match those calculated with Eq. (6.2.5) of Ref. 8 (column 3 of Table 3, columns 3 and 5 of Table 4). Specifically, the imaginary parts of the distant saddle points differ considerably. Until θ exceeds 2, the imaginary parts are separated by at least 0.1. In fact, the greatest disparity occurs near $\theta = 1$, where apparently the roots of Oughstun's polynomial approach $\infty - 1.1200i = \infty - 4\delta i$. This value is estimated by determining the roots for $1 < \theta < 1.009$. Clearly, this disagrees with the theoretically predicted value of $\infty - 2\delta i$; whereas from Eq. (59), the limiting value of ω_{D1} as $\theta \rightarrow 1+$ is in agreement with the theoretical prediction. Similarly, for the near saddle points (ω_{N1} and ω_{N2}), the difference between the roots is largest at $\theta = 1$ and gradually diminishes as θ increases. As Oughstun and Sherman note, $\omega_{D1} \rightarrow \omega'_+ \doteq (5.9935 - 0.2800i) \times 10^{16}$ and $\omega_{N1} \rightarrow \omega'_+ \doteq (3.9902 - 0.2800i) \times 10^{16}$ as θ approaches infinity. In addition, the critical value θ_1 , where the near saddle points change from pure imaginary to being symmetrically located on either side of the imaginary axis, is 1.502735905 to eight decimal places.

Although the numerical evaluations of the roots via Eq. (59) differ from roots that are computed with the eighth-degree polynomial of Oughstun and Sherman, they do match the figures on pages 236–238 of Ref. 8. Consequently, the authors suspect that in calculating the “exact” roots for their figures, Oughstun and Sherman applied Newton's method to an equation other than the polynomial given by Eq. (6.2.5).

4.3 Contributions from Distant Saddle Points

In this section, a uniform asymptotic approximation of $\mathcal{A}_S(z, \theta)$ is obtained by following the derivations in Ref. 7 and Section 7.2 of Ref. 8. From Theorem 5.4 of Ref. 8, a restatement of a theorem in Ref. 27, a uniform asymptotic expansion of $\mathcal{A}_S(z, \theta, T_0)$ to first order is

$$\mathcal{A}_S(z, \theta, T_0) = -\frac{U(\theta_{T_0})}{2\pi} \operatorname{Re} \left[e^{-i\omega_c T_0} \int_{P_D(\theta)} \frac{T(\omega)}{\omega - \omega_c} e^{\frac{z}{\epsilon} \phi(\omega, \theta_{T_0})} d\omega \right] \quad (60a)$$

$$\begin{aligned} \approx U(\theta_{T_0}) \operatorname{Re} \left[e^{-iz\beta(\theta_{T_0})} [2\alpha(\theta_{T_0})e^{-i\frac{\pi}{2}}]^\nu \left[\gamma_0(\theta_{T_0}) J_\nu(z\alpha(\theta_{T_0})) \right. \right. \\ \left. \left. + 2\alpha(\theta_{T_0})e^{-i\frac{\pi}{2}} \gamma_1(\theta_{T_0}) J_{\nu+1}(z\alpha(\theta_{T_0})) \right] \right], \end{aligned} \quad (60b)$$

where J_ν and $J_{\nu+1}$ are Bessel functions,

$$\tilde{v}(\omega) = \frac{i}{\omega}, \quad (61a)$$

$$\alpha(\theta_{T_0}) = \frac{i}{2c} [\phi(\omega_{D1}, \theta_{T_0}) - \phi(\omega_{D2}, \theta_{T_0})], \quad (61b)$$

$$\beta(\theta_{T_0}) = \frac{i}{2c} [\phi(\omega_{D1}, \theta_{T_0}) + \phi(\omega_{D2}, \theta_{T_0})], \quad (61c)$$

$$\begin{aligned} \gamma_0(\theta_{T_0}) = & \frac{1}{2} \left\{ \tilde{v}(\omega_{D1}(\theta_{T_0}) - \omega_c) \left[\frac{1}{2\alpha(\theta_{T_0})} \right]^{1+\nu} T(\omega_{D1}(\theta_{T_0})) \left[\frac{4c\alpha^3(\theta_{T_0})}{i\phi_{\omega\omega}(\omega_{D1}(\theta_{T_0}), \theta_{T_0})} \right]^{\frac{1}{2}} \right. \\ & \left. + \tilde{v}(\omega_{D2}(\theta_{T_0}) - \omega_c) \left[\frac{-1}{2\alpha(\theta_{T_0})} \right]^{1+\nu} T(\omega_{D2}(\theta_{T_0})) \left[\frac{-4c\alpha^3(\theta_{T_0})}{i\phi_{\omega\omega}(\omega_{D2}(\theta_{T_0}), \theta_{T_0})} \right]^{\frac{1}{2}} \right\}, \end{aligned} \quad (61d)$$

$$\begin{aligned} \gamma_1(\theta_{T_0}) = & \frac{1}{4\alpha(\theta_{T_0})} \left\{ \tilde{v}(\omega_{D1}(\theta_{T_0}) - \omega_c) \left[\frac{1}{2\alpha(\theta_{T_0})} \right]^{1+\nu} T(\omega_{D1}(\theta_{T_0})) \left[\frac{4c\alpha^3(\theta_{T_0})}{i\phi_{\omega\omega}(\omega_{D1}(\theta_{T_0}), \theta_{T_0})} \right]^{\frac{1}{2}} \right. \\ & \left. - \tilde{v}(\omega_{D2}(\theta_{T_0}) - \omega_c) \left[\frac{-1}{2\alpha(\theta_{T_0})} \right]^{1+\nu} T(\omega_{D2}(\theta_{T_0})) \left[\frac{-4c\alpha^3(\theta_{T_0})}{i\phi_{\omega\omega}(\omega_{D2}(\theta_{T_0}), \theta_{T_0})} \right]^{\frac{1}{2}} \right\}. \end{aligned} \quad (61e)$$

The subscript $\omega\omega$ of ϕ denotes the second partial derivative of ϕ with respect to ω , and ν is a real number such that $T(\omega)/(\omega - \omega_c) = \omega^{-(1+\nu)} \tilde{g}(\omega)$ and \tilde{g} has a convergent Laurent series about $\omega = 0$. For the window function of Eq. (12), $\nu = 0$. The function \tilde{v} corresponds to \tilde{u} in Eqs. (7.2.13–15) of Ref. 8. When one sets $T(\omega_{Dj}(\theta_{T_0})) \equiv 1$ and identifies α and β with α/c and β/c of Ref. 8, Eqs. (60) and (61) reduce to Eqs. (7.2.11–15) of Ref. 8. The reason for this slight difference in nomenclature is that Oughstun and Sherman normalize the α and β of Theorem 5.4 [8] with division by c . Regardless, the final results are equivalent when the transmission coefficient is unity.

The approach taken in Section 7.2 of Ref. 8 approximates the expressions in Eqs. (61) directly; however, Theorem 5.4 actually provides some asymptotic approximations for α , β , and the radical in Eqs. (61). Before proceeding, the authors believe that Eqs. (5.4.10–12) of Ref. 8 and Eqs. (3.4.10–12) of Ref. 4 are not quite correct as a consequence of errors in some works of Handelsman and Bleistein [37]. These errors have been corrected on page 390 of Ref. 25 and result in the following modifications to expressions that occur in pertinent works of Oughstun and Sherman,

$$\alpha(\theta) = 2[-a_1(\theta)(\theta - 1)]^{\frac{1}{2}} + O((\theta - 1)^{\frac{3}{2}}), \quad (62a)$$

$$\beta(\theta) = a_0(\theta) + O((\theta - 1)), \quad (62b)$$

$$\left(\mp \frac{4\alpha^3(\theta)}{\psi^{(2)}(\omega_{\pm}, \theta)} \right)^{\frac{1}{2}} = 4|a_1(\theta)| \left[1 + O((\theta - 1)^{\frac{1}{2}}) \right]. \quad (62c)$$

As Eqs. (61) indicate, one derives an approximation to $\mathcal{A}_S(z, \theta, T_0)$ by developing accurate estimates of the distant saddle points and generalized phase. According to the so-called *second approximation to the distant saddle points* [38,39],

$$\omega_{D1}(\theta_{T_0}) \doteq \xi(\theta_{T_0}) - i\delta[1 + \eta(\theta_{T_0})], \quad (63a)$$

$$\omega_{D2}(\theta_{T_0}) \doteq -\xi(\theta_{T_0}) - i\delta[1 + \eta(\theta_{T_0})], \quad (63b)$$

$$\phi(\omega, \theta) \doteq i\omega(1 - \theta) - \frac{ib^2}{2(\omega + i\delta)}, \quad (63c)$$

where

$$\xi(\theta_{T_0}) = \left[\omega_0^2 - \delta^2 + \frac{b^2 \theta_{T_0}^2}{\theta_{T_0}^2 - 1} \right]^{\frac{1}{2}}, \quad (64a)$$

$$\eta(\theta_{T_0}) = \xi^{-2}(\theta_{T_0}) \left[\frac{\delta^2}{27} + \frac{b^2}{\theta_{T_0}^2 - 1} \right]. \quad (64b)$$

Substituting Eqs. (63) and (64) into Eqs. (60) and (61) leads to more general versions of γ_0 , γ_1 , and A_S in Eqs. (7.2.13–15) of Ref. 8. In hindsight, one can obtain these generalizations by replacing $\tilde{u}(\omega_{SP_D^+} - \omega_c)$ and $\tilde{u}(\omega_{SP_D^-} - \omega_c)$ of Ref. 8 with $\tilde{v}(\omega_{D1} - \omega_c)T(\omega_{D1})$ and $\tilde{v}(\omega_{D2} - \omega_c)T(\omega_{D2})$, respectively. Let T_R , T_I , n_R , and n_I be the real and imaginary parts of the transmission coefficient ($T = T_R + iT_I$) and the refractive index ($n = n_R + in_I$); then by Eq. (20a),

$$T_R(\omega) = \frac{2(1 + n_R(\omega))}{(1 + n_R(\omega))^2 + n_I^2(\omega)} = \frac{2 \left[1 + \sqrt{\frac{\rho\rho'}{rr'}} \cos \left(\frac{\alpha+\alpha'-\psi-\psi'}{2} \right) \right]}{1 + \frac{\rho\rho'}{rr'} + 2\sqrt{\frac{\rho\rho'}{rr'}} \cos \left(\frac{\alpha+\alpha'-\psi-\psi'}{2} \right)}, \quad (65a)$$

$$T_I(\omega) = \frac{-2n_I(\omega)}{(1 + n_R(\omega))^2 + n_I^2(\omega)} = \frac{-2\sqrt{\frac{\rho\rho'}{rr'}} \sin \left(\frac{\alpha+\alpha'-\psi-\psi'}{2} \right)}{1 + \frac{\rho\rho'}{rr'} + 2\sqrt{\frac{\rho\rho'}{rr'}} \cos \left(\frac{\alpha+\alpha'-\psi-\psi'}{2} \right)}, \quad (65b)$$

$$n_R(\omega_{D1,2}(\theta_{T_0})) \doteq 1 - \frac{b^2 \xi^{-2}(\theta_{T_0}) \left[1 + \delta^2 \xi^{-2}(\theta_{T_0}) [1 - \eta^2(\theta_{T_0})] \right]}{2 \left[1 + \delta^2 \xi^{-2}(\theta_{T_0}) [1 + \eta(\theta_{T_0})] \right]^2 \left[1 + \delta^2 \xi^{-2}(\theta_{T_0}) [1 - \eta(\theta_{T_0})] \right]^2}, \quad (65c)$$

$$n_I(\omega_{D1,2}(\theta_{T_0})) \doteq \frac{\mp 2\delta b^2 \xi^{-3}(\theta_{T_0}) \eta(\theta_{T_0})}{2 \left[1 + \delta^2 \xi^{-2}(\theta_{T_0}) [1 + \eta(\theta_{T_0})] \right]^2 \left[1 + \delta^2 \xi^{-2}(\theta_{T_0}) [1 - \eta(\theta_{T_0})] \right]^2}. \quad (65d)$$

The dependencies of the right sides of Eqs. (65(a) and (b)) on ω are not shown explicitly but are specified by Eqs. (19). In comparing Eqs. (65(a) and (b)) and Eq. (20(b)), note that the imaginary parts of $T(\omega)$ and $R(\omega)$ are equal and that $T(\omega) - R(\omega) = \text{Re}[T(\omega) - R(\omega)] \equiv 1$. Moreover, the approximations for n_R at $\omega_{D1}(\theta_{T_0})$ and $\omega_{D2}(\theta_{T_0})$ are equal; however the minus and plus signs in Eq. (65(d)) correspond to n_I evaluated at $\omega_{D1}(\theta_{T_0})$ and $\omega_{D2}(\theta_{T_0})$, respectively.

Finally, by substituting Eqs. (63) and (65) into Eqs. (60) and (61), one obtains

$$\begin{aligned}
 \mathcal{A}_S(z, \theta, T_0) \doteq U(\theta_{T_0}) \frac{\xi(\theta_{T_0})}{2b} & \left[\theta_{T_0} - 1 + \frac{b^2}{2} \frac{1}{\xi^2(\theta_{T_0}) + \delta^2[1 - \eta(\theta_{T_0})]^2} \right]^{\frac{1}{2}} \\
 & \times e^{-\frac{z\xi(\theta_{T_0})}{c} \left[[\theta_{T_0} - 1][1 + \eta(\theta_{T_0})] + \frac{b^2}{2} \frac{1 - \eta(\theta_{T_0})}{\xi^2(\theta_{T_0}) + \delta^2[1 - \eta(\theta_{T_0})]^2} \right]} \\
 & \times \left\{ \left(- \frac{T_R(\omega_{D1}(\theta_{T_0})) \left[\frac{3}{2} \delta [\xi(\theta_{T_0}) - \omega_c][1 - \eta(\theta_{T_0})] + \delta \xi(\theta_{T_0})[1 + \eta(\theta_{T_0})] \right]}{[\xi(\theta_{T_0}) - \omega_c]^2 + \delta^2[1 + \eta(\theta_{T_0})]^2} \right. \right. \\
 & \quad - \frac{T_I(\omega_{D1}(\theta_{T_0})) \left[\xi(\theta_{T_0})[\xi(\theta_{T_0}) - \omega_c] - \frac{3}{2} \delta^2[1 - \eta^2(\theta_{T_0})] \right]}{[\xi(\theta_{T_0}) - \omega_c]^2 + \delta^2[1 + \eta(\theta_{T_0})]^2} \\
 & \quad + \frac{T_R(\omega_{D1}(\theta_{T_0})) \left[\frac{3}{2} \delta [\xi(\theta_{T_0}) + \omega_c][1 - \eta(\theta_{T_0})] + \delta \xi(\theta_{T_0})[1 + \eta(\theta_{T_0})] \right]}{[\xi(\theta_{T_0}) + \omega_c]^2 + \delta^2[1 + \eta(\theta_{T_0})]^2} \\
 & \quad + \frac{T_I(\omega_{D1}(\theta_{T_0})) \left[\xi(\theta_{T_0})[\xi(\theta_{T_0}) + \omega_c] - \frac{3}{2} \delta^2[1 - \eta^2(\theta_{T_0})] \right]}{[\xi(\theta_{T_0}) + \omega_c]^2 + \delta^2[1 + \eta(\theta_{T_0})]^2} \Big) \\
 & \quad \times J_0 \left(\frac{z\xi(\theta_{T_0})}{c} \left[\theta_{T_0} - 1 + \frac{b^2}{2} \frac{1}{\xi^2(\theta_{T_0}) + \delta^2[1 - \eta(\theta_{T_0})]^2} \right] \right) \\
 & \quad + \left(\frac{T_R(\omega_{D1}(\theta_{T_0})) \left[\xi(\theta_{T_0})[\xi(\theta_{T_0}) - \omega_c] - \frac{3}{2} \delta^2[1 - \eta^2(\theta_{T_0})] \right]}{[\xi(\theta_{T_0}) - \omega_c]^2 + \delta^2[1 + \eta(\theta_{T_0})]^2} \right. \\
 & \quad \quad - \frac{T_I(\omega_{D1}(\theta_{T_0})) \left[\frac{3}{2} \delta [\xi(\theta_{T_0}) - \omega_c][1 - \eta(\theta_{T_0})] + \delta \xi(\theta_{T_0})[1 + \eta(\theta_{T_0})] \right]}{[\xi(\theta_{T_0}) - \omega_c]^2 + \delta^2[1 + \eta(\theta_{T_0})]^2} \\
 & \quad \quad - \frac{T_R(\omega_{D1}(\theta_{T_0})) \left[\xi(\theta_{T_0})[\xi(\theta_{T_0}) + \omega_c] - \frac{3}{2} \delta^2[1 - \eta^2(\theta_{T_0})] \right]}{[\xi(\theta_{T_0}) + \omega_c]^2 + \delta^2[1 + \eta(\theta_{T_0})]^2} \\
 & \quad \quad + \frac{T_I(\omega_{D1}(\theta_{T_0})) \left[\frac{3}{2} \delta [\xi(\theta_{T_0}) + \omega_c][1 - \eta(\theta_{T_0})] + \delta \xi(\theta_{T_0})[1 + \eta(\theta_{T_0})] \right]}{[\xi(\theta_{T_0}) + \omega_c]^2 + \delta^2[1 + \eta(\theta_{T_0})]^2} \Big) \\
 & \quad \times J_1 \left(\frac{z\xi(\theta_{T_0})}{c} \left[\theta_{T_0} - 1 + \frac{b^2}{2} \frac{1}{\xi^2(\theta_{T_0}) + \delta^2[1 - \eta(\theta_{T_0})]^2} \right] \right) \Big) \Big\}. \quad (66)
 \end{aligned}$$

In the limit as $T_R \rightarrow 1$ and $T_I \rightarrow 0$, $\mathcal{A}_S(z, \theta, T_0)$ reduces to Eq. (7.2.24) of Ref. 8. The effect of T on \mathcal{A}_S is negligible because $T \doteq 1$ for the extremely high frequencies associated with this precursor.

4.4 Example of Transmitted Field

The contributions $\mathcal{A}_S(z, \theta)$ to the transmitted field from the distant saddle points $\{\omega_{D1}, \omega_{D2}\}$ are evaluated and plotted for the observation point at $z = 10^{-5}$ m in the Lorentz medium, for Brillouin's values of the physical constants ($\omega_0 = 4.0 \times 10^{16}$ s $^{-1}$, $b^2 = 20.0 \times 10^{32}$ s $^{-2}$, $\delta = 0.28 \times 10^{16}$ s $^{-1}$), and for an incident plane wave that consists of a single cycle of the sine at angular carrier frequency $\omega_c = 10^{16}$ s $^{-1}$. With this choice of parameters, the medium is highly absorptive about ω_0 , and ω_c ($T_0 = 2\pi/\omega_c$) is below the medium's absorption band, $((\omega_0^2 - \delta^2)^{1/2}, (\omega_1^2 - \delta^2)^{1/2})$.

The results for \mathcal{A}_S are then compared to the contributions given by Eq. (7.2.24) of Ref. 8, where Oughstun and Sherman's representation of the Sommerfeld precursor is designated $\mathcal{A}_{SO}(z, \theta)$.

Graphs of $\mathcal{A}_S(z, \theta, 0)$ and $\mathcal{A}_S(z, \theta, T_0)$ versus normalized time θ are shown in Figs. 9(a) and (b), respectively. As one expects from Eqs. (49), (56), and (60), $\mathcal{A}_S(z, \theta, T_0)$ is $\mathcal{A}_S(z, \theta, 0)$ delayed by $cT_0/z \doteq 0.0188365$. On inspection, the plot of $\mathcal{A}_S(z, \theta, 0)$ looks like Fig. 6 of Ref. 8. By substituting $T_0 = 0$ in Eq. (66) and by manipulating Eqs. (63–66), one can argue that the envelope of $\mathcal{A}_S(z, \theta, 0)$ in Fig. 9(a) behaves like

$$\pm(\theta - 1)e^{-(z\delta/c)[\theta^{-2}(\theta^2+1)(\theta-1)+(2\theta^2)^{-1}(\theta+1)^2(\theta-1)^2]}. \quad (67a)$$

Note that the exponent has linear and quadratic terms in $(\theta - 1)$. For θ near 1, the exponent is dominated by the linear term, and Eq. (67a) becomes

$$\pm(\theta - 1)e^{-(2z\delta/c)(\theta-1)}, \quad (67b)$$

which is proportional to the Gaussian probability density function with parameters 2 and $c/(2z\delta)$ [40]. On the other hand, when θ is large, the envelope behaves like the Rayleigh probability density

$$\pm(\theta - 1)e^{-(z\delta/(2c))(\theta-1)^2}. \quad (67c)$$

Recall that $\mathcal{A}_S(z, \theta) = \mathcal{A}_S(z, \theta, 0) - \mathcal{A}_S(z, \theta, T_0)$. When this difference is plotted, one observes two slightly overlapped signal packets (Fig. 9(c)), which correspond to the intervals $1 \leq \theta \leq cT_0/z$ and $\theta > cT_0/z$. In the first packet ($1 \leq \theta \leq cT_0/z$), $\mathcal{A}_S(z, \theta) = \mathcal{A}_S(z, \theta, 0)$ since $\mathcal{A}_S(z, \theta, T_0) \equiv 0$. Moreover, at $\theta = cT_0/z$, the magnitude of $\mathcal{A}_S(z, \theta)$ has decreased roughly to one tenth of its maximum value. When $\theta > cT_0/z$, the contribution from $\mathcal{A}_S(z, \theta, 0)$ decreases as θ increases. However, until $\mathcal{A}_S(z, \theta, 0)$ becomes negligible near $\theta = 1.04$, the trailing edge of the first packet interferes with the leading edge of the second packet, thereby, producing the uneven behavior of the second packet's envelope. On comparing Fig. 9(c) to the first part of the bottom frame of Fig. 15 in Ref. 7, the curves appear to be very similar. To ascertain the degree of similarity between \mathcal{A}_S and \mathcal{A}_{SO} , the difference $\mathcal{A}_S(z, \theta) - \mathcal{A}_{SO}(z, \theta)$ is plotted in Fig. 9(d). As the figure indicates, the absolute difference is always less than 0.000004. Thus the graph of \mathcal{A}_S is visually indistinguishable from \mathcal{A}_{SO} . The reason for this lies in the behavior of $T(\omega_{D1}(\theta))$. According to Table A1 of the Appendix,

$$1 \leq T_R(\omega_{D1}(\theta)) \leq 1.02 \quad \text{and} \quad 0 \leq T_I(\omega_{D1}(\theta)) \leq 0.00062, \quad (68)$$

for $1 \leq \theta \leq 1.05$, which implies that $T_R \doteq 1$ and $T_I \doteq 0$ at values of θ for which the Sommerfeld precursor is significant. On the other hand, the decay of the exponential factor completely dominates the contribution from the variations in $T(\omega_{D1}(\theta))$ when θ exceeds 1.05 since T is bounded. Hence choosing $T(\omega_{D1}(\theta)) \doteq 1$ in Eq. (66) has a negligible effect, and the small excursions of the transmission coefficient from unity at optical frequencies for Brillouin's constants have little impact on \mathcal{A}_S . This analysis merely validates the tacit assumption that $T \equiv 1$ at optical frequencies for the Sommerfeld precursor. Of course, one expects the impact of $T(\omega)$ on \mathcal{A}_S to be different, perhaps more significant, over other frequency regimes like millimeter waves or microwaves.

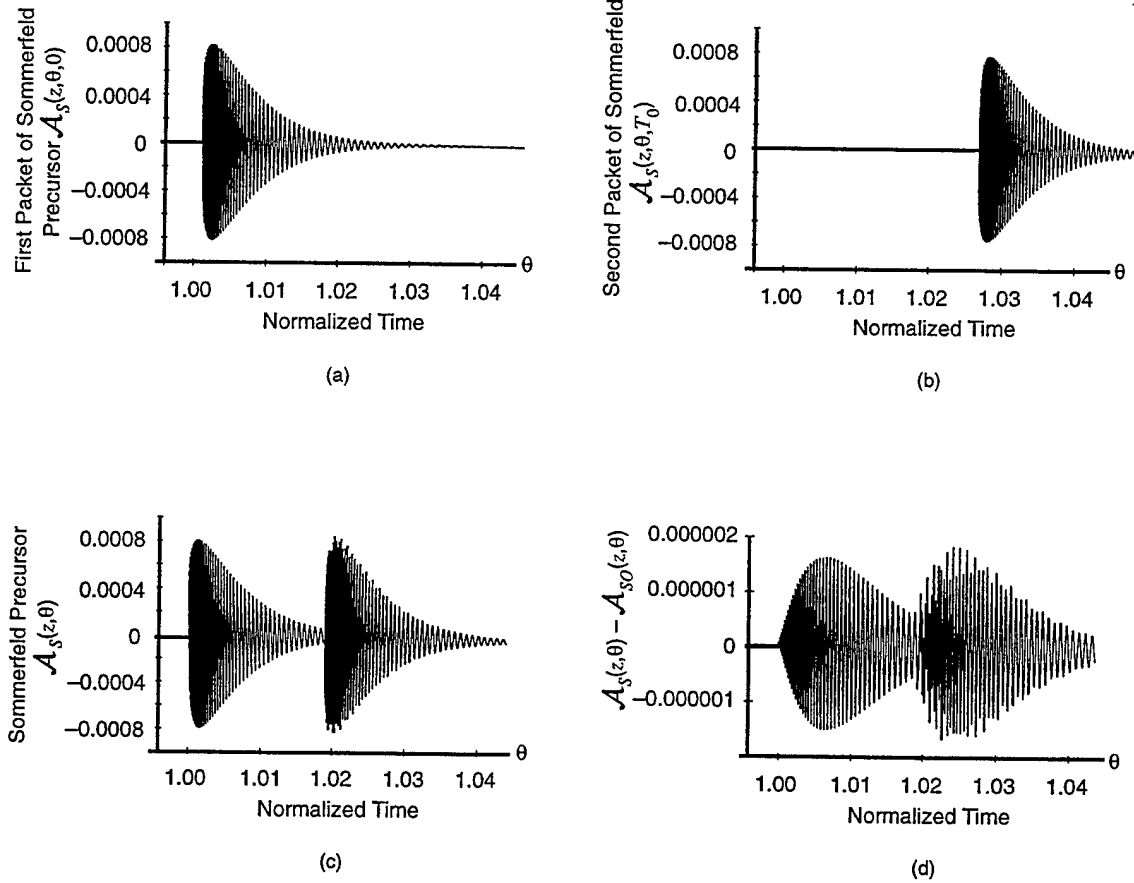


Fig. 9 – Sommerfeld precursor and associated functions versus normalized time θ at $z = -10^{-5}$ m in the Lorentz medium with $\omega_0 = 4.0 \times 10^{16} \text{ s}^{-1}$, $b^2 = 20.0 \times 10^{32} \text{ s}^{-2}$, and $\delta = 0.28 \times 10^{16} \text{ s}^{-1}$: (a) $\mathcal{A}_S(z, \theta, 0)$, (b) $\mathcal{A}_S(z, \theta, T_0)$, (c) $\mathcal{A}_S(z, \theta) = \mathcal{A}_S(z, \theta, 0) - \mathcal{A}_S(z, \theta, T_0)$, and (d) $\mathcal{A}_S(z, \theta) - \mathcal{A}_{SO}(z, \theta)$. The incident pulsed field is a single-cycle sine at $\omega_c = 10^{16} \text{ s}^{-1}$ with $T_0 = 2\pi/\omega_c$, and \mathcal{A}_{SO} is \mathcal{A}_S evaluated at $T_R(\omega) \equiv 1$ and $T_I(\omega) \equiv 0$.

As stated in the introduction, the lengthy endeavor of deriving \mathcal{A}_B and \mathcal{A}_C for all eventualities is not addressed. However, some comments are made regarding the impact of the transmission coefficient on \mathcal{A}_B and \mathcal{A}_C . By Eqs. (57) and (58), the inclusion of $T(\omega)$ affects the amplitudes of \mathcal{A}_B and \mathcal{A}_C and not their durations. By extrapolating from Figs. 8 and 10 of Ref. 7, one deduces that the supports/peak magnitudes [41] of \mathcal{A}_B and \mathcal{A}_C are approximately $1.43 \leq \theta \leq 1.62/0.12$ and $1.44 \leq \theta \leq 1.70/0.005$, respectively. Further, by Fig. A2 and some calculations, \mathcal{A}_S is negligible for $\theta > 1.08$. Consequently, the transmitted field has a significant nonzero value for θ in $[1, 1.08]$, $[1.43, 1.62]$, or $[1.44, 1.70]$. Although further observations on \mathcal{A}_B and \mathcal{A}_C can be made only after detailed study, one more conclusion regarding \mathcal{A}_C can be drawn. Since $T(\omega_c) \doteq 0.7914 - 0.0051i$ is a multiplicative factor in the residue

$$T(\omega_c) e^{(z/c)\phi(\omega_c, \theta_{T_0})} \quad (69)$$

of \mathcal{A}_C and since $T(\omega_c)$ differs substantially from unity, the inclusion of $T(\omega_c)$ in evaluating \mathcal{A}_C will result in a 21% decrease in the main signal's amplitude as computed by Ref. 7.

To compare \mathcal{A}_S to E_y^r , consider Fig. 6(d), which depicts E_y^r at an equal distance from the dispersive medium. The reflected field is essentially nonzero for θ in $[1, 1.03]$ and has a peak value of 0.21016 at $\theta \doteq 1.0142$, which is significant relative to the derived and expected components of E_y^t . According to Table 2, this corresponds nicely to the value of $|\text{Re}[R(\omega_c)]|$. Furthermore, $|\text{Re}[R(\omega_c)]|$ is consistent with the predicted 21% percent decrement of \mathcal{A}_C . Intuitively, one expects this because $T(\omega_c) - R(\omega_c) \equiv 1$. The comparison between the expected strengths and durations of E_y^r and E_y^t in this example provides a compelling argument for including the frequency dependence of the reflection and transmission coefficients in formulating this propagation problem, even for fields at optical frequencies.

5. SUMMARY AND CONCLUSIONS

This report generalizes the formulations of Sommerfeld, Brillouin, and Oughstun and Sherman for one-dimensional propagation of pulsed fields at optical frequencies in a medium for which the Lorentz model is valid and for which the Lorentz absorption frequency δ is less than its resonance frequency ω_0 . The generalizations are: (1) providing a formulation that is applicable to frequencies for which the Lorentz model of the medium is appropriate; (2) accomodating a pulsed source outside the Lorentz medium instead of specifying the field on the medium's boundary; (3) accounting for reflection from the medium; and (4) including a frequency-dependent transmission coefficient in the transmitted field. Specifically, results are obtained for the case when the source is a rectangularly modulated sine function at angular carrier frequency ω_c and when the duration T_0 of the source is a positive integer multiple of $2\pi/\omega_c$. Moreover, results on the reflected and transmitted fields are obtained for Brillouin's choice of Lorentz parameters (ω_0, δ, b) . This example demonstrates the necessity of including the transmission and reflection coefficients for this class of propagation problems.

An exact expression for the time-domain reflected field, that is amenable to physical interpretation and numerical evaluation, is derived. When time $t = 0$ is designated as the instant the incident field reaches the medium's boundary, the reflected field is first observed at a point a distance $|z|$ from this boundary at time $|z|/c$. The field consists of two components: (1) a sine function, $|R(\omega_c)| \sin(\omega_c \hat{t} - \arg[R(\omega_c)])$, which comes from the pole contributions to the inversion integral and has the same duration T_0 as the incident field (R is the reflection coefficient); and (2) two exponentially damped sinusoidal terms, which come from the branch-cut contributions, with time-dependent phases that broaden the incident pulse and cause ringing in the trailing edge. The behavior of the reflected field changes with the value of ω_c relative to ω_0 . As ω_c increases, the field evolves from a reduced, negative replica of the incident field for $\omega_c \leq \omega_0/10$ to a much broader field with an increasingly distorted leading edge and a damped trailing edge having a greater number of zero crossings at the higher carrier frequencies. For $\omega_c \leq 3\omega_0$, the reflected field's amplitude is significant, even for optical frequencies. In addition, early-time and high-frequency fields are developed, and they are shown to be in excellent agreement over a short time for a particular optical example. The high-frequency field extends Colby's result by including the attenuation factor δ , which also adds higher-order temporal terms. The inclusion of these terms improves the accuracy of Colby's result.

By following the methodology of Oughstun and Sherman, the time-domain transmitted fields are expressed as the sum of three components: the Sommerfeld precursor, the Brillouin precursor, and the main signal. Rather than derive uniform asymptotic representations of all three components of the transmitted field, a uniform asymptotic approximation of the Sommerfeld precursor is

developed to illustrate the impact of the transmission coefficient on the field. Moreover, the Sommerfeld precursor is shown to reduce to the results of Oughstun and Sherman when the transmission coefficient is unity.

The derived theoretical results are made more concrete by applying them for Brillouin's choice of the Lorentz medium's parameters and for Oughstun's choice of carrier frequency. Specifically, the reflected field and Sommerfeld precursor are obtained at distance $|z|$ from the medium's boundary. When the incident pulsed field is a single cycle of the sine function ($T_0 = 2\pi/\omega_c$), neither field is observed until t exceeds $|z|c^{-1}$. The Sommerfeld precursor has a significant value for $|z|c^{-1} < t < |z|c^{-1} + 4T_0$ and consists of two slightly overlapped wave packets. The envelope of each packet has a leading edge that resembles the Gamma probability density function, has a trailing edge similar to the Rayleigh density function, and bounds a highly oscillatory field. The transmission coefficient has a negligible effect on the Sommerfeld precursor because it consists of extremely high frequencies; however, a heuristic analysis implies that its impact on the main signal is significant. In contrast, the reflected field is a distorted version of the negative of the incident field and has an amplitude that is 21% of the incident field's amplitude and is roughly 250 times the peak of the Sommerfeld precursor's envelope. Further, the reflected field's support essentially is $|z|c^{-1} < t < |z|c^{-1} + 1.5T_0$, which is 37.5% of the precursor's support. Given these facts, one is drawn to the conclusion: accurate analyses of problems involving propagation of a pulsed field that is externally incident on a Lorentz medium require frequency-dependent reflection and transmission coefficients.

6. ACKNOWLEDGMENT

The authors thank F.C. Lin for providing some computations with *MATLAB*. This work was sponsored by the Naval Research Laboratory and the Office of Naval Research.

REFERENCES

1. A. Sommerfeld, *Ann. Phys. (Leipzig)* **44**(10), 177–202 (1914).
2. L. Brillouin, *Ann. Phys. (Leipzig)* **44**(10), 203–240 (1914).
3. L. Brillouin, *Wave Propagation and Group Velocity* (Academic Press, New York, 1960).
4. K.E. Oughstun, "Propagation of Optical Pulses in Dispersive Media," Doctoral dissertation, The University of Rochester, Rochester, N.Y., 1978.
5. K.E. Oughstun and G.C. Sherman, *J. Opt. Soc. Am. B* **5**(4), 817–849 (1988).
6. K.E. Oughstun and G.C. Sherman, *J. Opt. Soc. Am. A* **6**(9), 1394–1420 (1989).
7. K.E. Oughstun and G.C. Sherman, *Phys. Rev. A* **41**(11), 6090–6113 (1990).
8. K.E. Oughstun and G.C. Sherman, *Electromagnetic Pulse Propagation in Causal Dielectrics* (Springer-Verlag, Berlin, 1994).
9. A radar is defined to be ultrawideband (UWB) when its fractional bandwidth exceeds 25%, according to the executive summary of the OSD/DARPA study, *Assessment of Ultra-Wideband (UWB) Technology*, in the *IEEE Aer. and El. Mag.*, November, 1990, pp. 45–49.
10. B. Noel, ed., *Ultra-Wideband Radar: Proceedings of the First Los Alamos Symposium* (CRC, Boca Raton, Fla., 1991).

11. H.L. Bertoni, L. Carin, and L.B. Felsen, eds., *Ultra-Wideband, Short-Pulse Electromagnetics* (Plenum, New York, 1993).
12. L.Yu. Astanin, A.A. Kostylev, Yu.S. Zinoviev, and A.Ya. Pasmurov, *Radar Target Characteristics: Measurements and Applications* (CRC, Boca Raton, Fla., 1994).
13. J.D. Taylor, ed., *Introduction to Ultra-Wideband Radar Systems* (CRC, Boca Raton, Fla., 1995).
14. L. Carin and L.B. Felsen, eds., *Ultra-Wideband, Short-Pulse Electromagnetics 2* (Plenum, N.Y., 1995).
15. W. Colby, *Phys. Rev.* **V**(3), 253–265 (1915).
16. A. Sommerfeld, *Ann. Phys. (Leipzig)* **44**(10), 190 (1914).
17. L. Brillouin, *Wave Propagation and Group Velocity* (Academic Press, N.Y., 1960), Ch. III, pp. 56–57; and K.E. Oughstun and G.C. Sherman, *Electromagnetic Pulse Propagation in Causal Dielectrics* (Springer-Verlag, Berlin, 1994), Ch. 6, p. 234.
18. The fractional bandwidth B_F of the single-cycle sine function is given by the formula, $B_F = [2(\omega_U - \omega_L)/(\omega_U + \omega_L)] \times 100\%$, where ω_U and ω_L are the upper and lower frequencies of the passband of the power spectral density of the single-cycle sine, $4\omega_c^2 \sin^2(\pi\omega/\omega_c)/(\omega_c^2 - \omega^2)^2$. If one uses the half-power criterion to determine the passband, then $\omega_U \doteq 1.309\omega_c$ and $\omega_L \doteq 0.411\omega_c$. Hence $B_F \doteq 104\%$, which is ultrawideband according to Ref. 9.
19. L.L. Pennisi, *Elements of Complex Variables* (Holt, Rinehart, and Winston, New York, 1963), p. 185.
20. W. Colby, *Phys. Rev.* **V**(3), 264 (1915).
21. A. Erdelyi, *Asymptotic Expansions* (Dover, New York, 1956), Ch. II, pp. 29 and 36.
22. F.W.J. Olver, *Asymptotics and Special Functions* (Academic Press, New York, 1974), Ch. 3, p. 80.
23. E.T. Copson, *Asymptotic Expansions* (Cambridge, London, 1965), Ch. 10, pp. 107–117.
24. N. Bleistein and R. Handelsman, *Asymptotic Expansions of Integrals* (Holt, Rinehart, and Winston, New York, 1975), Ch. 9, pp. 367–410.
25. N. Bleistein and R. Handelsman, *Asymptotic Expansions of Integrals* (Dover, New York, 1986), Ch. 9, pp. 367–410.
26. A. Erdelyi, “Uniform Asymptotic Expansion of Integrals,” in *Analytical Methods in Mathematical Physics*, R.P. Gilbert and R.G. Newton, eds. (Gordon and Breach, New York, 1970), pp. 149–168.
27. R.A. Handelsman and N. Bleistein, *Arch. Ration. Mech. Anal.* **35**, 267–283 (1969).
28. K.E. Oughstun, “Propagation of Optical Pulses in Dispersive Media,” Doctoral dissertation, The University of Rochester, Rochester, N.Y., 1978, Ch. 2; and K.E. Oughstun and G.C. Sherman, *Electromagnetic Pulse Propagation in Causal Dielectrics* (Springer-Verlag, Berlin, 1994), Ch. V, p. 141.
29. K.E. Oughstun and G.C. Sherman, *Electromagnetic Pulse Propagation in Causal Dielectrics* (Springer-Verlag, Berlin, 1994), Ch. 5, Secs. 6.5 and 7.2.1.

30. K.E. Oughstun and G.C. Sherman, *Electromagnetic Pulse Propagation in Causal Dielectrics* (Springer-Verlag, Berlin, 1994), Ch. 5, p. 168 and Ch. 7, p. 281.
31. K.E. Oughstun and G.C. Sherman, *Electromagnetic Pulse Propagation in Causal Dielectrics* (Springer-Verlag, Berlin, 1994), Ch. 6, pp. 245–248.
32. F.W.J. Olver, *SIAM Rev.* **12**(2), 228–247 (1970).
33. C. Chester, B. Friedman, and F. Ursell, *Proc. Cambridge Philos. Soc.* **53**, 599–611 (1957).
34. N. Bleistein, *Commun. Pure Appl. Math.* **XIX**(4), 353–370 (1966).
35. N. Bleistein, *J. Math. Mech.* **17**(6), 533–559 (1967).
36. K.E. Oughstun and G.C. Sherman, *Electromagnetic Pulse Propagation in Causal Dielectrics* (Springer-Verlag, Berlin, 1994), Ch. 6, pp. 192–249.
37. N. Bleistein and R. Handelsman, *Asymptotic Expansions of Integrals* (Holt, Rinehart, and Winston, New York, 1975), Ch. 9, p. 390; and R.A. Handelsman and N. Bleistein, *Arch. Ration. Mech. Anal.* **35**, 267–283 (1969).
38. K.E. Oughstun and G.C. Sherman, *Electromagnetic Pulse Propagation in Causal Dielectrics* (Springer-Verlag, Berlin, 1994), Ch. 6, p. 214.
39. L. Brillouin, *Ann. Phys. (Leipzig)* **44**(10), 203–240 (1914), Eq. (16) on p. 212.
40. V.K. Rohatgi, *An Introduction to Probability Theory and Mathematical Statistics* (Wiley, New York, 1976), Ch. 5, p. 206.
41. The support of a real-valued function on the real line is the closure of the set of all points at which the function is nonzero.

Appendix

As evidenced in the Sections 2 through 4, the reflected and transmitted fields depend critically on n , R , and T . This appendix presents the behavior of each quantity throughout the cut complex plane (Fig. 2). Since the reflection and transmission coefficients are functions of the index of refraction, n is treated first.

The index of refraction is specified by Eqs. (6), (7), (19), and (20(a)). With $\omega = \omega' + i\omega''$,

$$|n(\omega)| = \left[\frac{[(\omega' + \omega_3)^2 + (\omega'' + \delta)^2] [(\omega' - \omega_3)^2 + (\omega'' + \delta)^2]}{[(\omega' + \omega_2)^2 + (\omega'' + \delta)^2] [(\omega' - \omega_2)^2 + (\omega'' + \delta)^2]} \right]^{\frac{1}{4}}, \quad (A1)$$

$$\alpha = \begin{cases} -\pi + \text{Arctan} \left(\frac{-(\omega'' + \delta)}{-(\omega' - \omega_3)} \right), & \omega' - \omega_3 < 0 \text{ and } \omega'' + \delta < 0 \\ -\frac{\pi}{2}, & \omega' - \omega_3 = 0 \text{ and } \omega'' + \delta < 0 \\ -\text{Arctan} \left(\frac{-(\omega'' + \delta)}{(\omega' - \omega_3)} \right), & \omega' - \omega_3 > 0 \text{ and } \omega'' + \delta < 0 \\ 0, & \omega' - \omega_3 > 0 \text{ and } \omega'' + \delta = 0 \\ \text{Arctan} \left(\frac{(\omega'' + \delta)}{(\omega' - \omega_3)} \right), & \omega' - \omega_3 > 0 \text{ and } \omega'' + \delta > 0 \\ \frac{\pi}{2}, & \omega' - \omega_3 = 0 \text{ and } \omega'' + \delta > 0 \\ \pi - \text{Arctan} \left(\frac{(\omega'' + \delta)}{-(\omega' - \omega_3)} \right), & \omega' - \omega_3 < 0 \text{ and } \omega'' + \delta > 0 \\ \pi, & \omega' - \omega_3 < 0 \text{ and } \omega'' + \delta = 0, \end{cases} \quad (A2)$$

$$\psi = \begin{cases} \pi + \text{Arctan} \left(\frac{-(\omega'' + \delta)}{-(\omega' - \omega_2)} \right), & \omega' - \omega_2 < 0 \text{ and } \omega'' + \delta < 0 \\ \frac{3\pi}{2}, & \omega' - \omega_2 = 0 \text{ and } \omega'' + \delta < 0 \\ 2\pi - \text{Arctan} \left(\frac{-(\omega'' + \delta)}{(\omega' - \omega_2)} \right), & \omega' - \omega_2 > 0 \text{ and } \omega'' + \delta < 0 \\ 0, & \omega' - \omega_2 > 0 \text{ and } \omega'' + \delta = 0 \\ \text{Arctan} \left(\frac{(\omega'' + \delta)}{(\omega' - \omega_2)} \right), & \omega' - \omega_2 > 0 \text{ and } \omega'' + \delta > 0 \\ \frac{\pi}{2}, & \omega' - \omega_2 = 0 \text{ and } \omega'' + \delta > 0 \\ \pi - \text{Arctan} \left(\frac{(\omega'' + \delta)}{-(\omega' - \omega_2)} \right), & \omega' - \omega_2 < 0 \text{ and } \omega'' + \delta > 0 \\ \pi, & \omega' - \omega_2 < 0 \text{ and } \omega'' + \delta = 0. \end{cases} \quad (A3)$$

One obtains the arguments α' and ψ' by replacing $\omega' - \omega_3$ and $\omega' - \omega_2$ with $\omega' + \omega_3$ and $\omega' + \omega_2$ in the expressions for α and ψ , respectively. The representations for $|n|$ and $(\alpha + \alpha' - \psi - \psi')/2$, given by Eqs. (A1)–(A3), are equivalent to the magnitude and argument of n in Eq. (6.1.14) of Ref. 8.

In the remainder of the Appendix, the horizontal (real) axis of each plot is normalized with a division by ω_0 ; that is, ω_0 corresponds to unity. Moreover, all figures are graphed for $\omega_c = 10^{16}$ rad/s and for Brillouin's values of ω_0 , b , and δ . Consequently, ω_c , b , δ , ω_2 , and ω_3 correspond to 0.25,

1.118, 0.07, 0.9975, and 1.4984, respectively. In addition, the branch points (ω'_- , ω_- , ω_+ , and ω'_+) are located approximately at $-1.4984 - 0.07i$, $-0.9975 - 0.07i$, $0.9975 - 0.07i$, and $1.4984 - 0.07i$. Although specific values of the physical parameters are chosen, the analysis is independent of these values, and the figures typify the behaviors of n , R , and T for any choice of ω_c , ω_0 , b , and δ under the constraint $\delta < \omega_0$.

Even though $n(\omega)$ is discontinuous across the branch cuts, setting $\omega'' = -i\delta$ in Eq. (A1) implies that $|n(\omega)|$ approaches 0 as $\omega \rightarrow \omega'_\pm$ and approaches $+\infty$ as $\omega \rightarrow \omega_\pm$. Further, one can argue that $|n(\omega)|$ has well-defined limits as ω approaches each point of the branch cuts. In particular,

$$\lim_{\omega \rightarrow a-i\delta} |n(\omega)| = \left[\frac{\omega_3^2 - a^2}{a^2 - \omega_2^2} \right]^{\frac{1}{2}}, \quad (\text{A4})$$

for a in $[-\omega_3, -\omega_2]$ or $[\omega_2, \omega_3]$. Consequently, $|n(\omega)|$ can be made continuous for ω in the complex plane except at ω_\pm , where the limits exist but are not finite. Both the 3-D (Fig. A1(a)) and cross-sectional (Fig. A2(a)) depictions illustrate the pronounced spikes at ω_\pm and the dips to zero at ω'_\pm . In the 3-D graph, the flat part of each peak is indicative of magnitude clipping at the value 2. Figure A1(a) provides a further illuminating glimpse of the behavior of $|n(\omega)|$ near the branch cuts by showing the cross section that is slightly above the cuts at $\omega'' = -0.0699\omega_0$. Clearly, away from the branch cuts, $|n(\omega)|$ is approximately unity. Specifically, for $|\omega| \geq 4\omega_0$, the calculated values of $|n|$ are within 0.01 of 1.

In Figs. A1(b) and A2(b), plots of the argument $(\alpha + \alpha' - \psi - \psi')/2$ of n indicate a jump discontinuity at each point along the line through the branch points ($\omega'' = -\delta$). In particular, as ω'' approaches $-\delta$ from above, $\arg[n(\omega)]$ approaches 0 for ω' in the intervals $(-\infty, \omega_3)$, $(-\omega_2, \omega_2)$, and $(\omega_3, +\infty)$, approaches $-\pi/2$ for ω' in $[-\omega_3, -\omega_2]$, and approaches $\pi/2$ for ω' in $[\omega_2, \omega_3]$. As ω'' approaches $-\delta$ from below, $\arg[n]$ approaches -2π for ω' in $(-\infty, \omega_3)$, $(-\omega_2, \omega_2)$, and $(\omega_3, +\infty)$, approaches $-3\pi/2$ for ω' in $[-\omega_3, -\omega_2]$, and approaches $-5\pi/2$ for ω' in $[\omega_2, \omega_3]$. These graphical observations are consistent with the entries of Table 1. Despite the discontinuous behavior of $\arg[n]$ along $\omega'' = -i\delta$, $e^{i\arg[n]/2}$ is continuous at each point of this line that is not on the cuts. Of course, one expects a difference between the values on the top and bottom of the cuts. With the choice of branch given by Eqs. (22), $e^{i\arg[n]/2}$ is $+i$ ($-i$) for the top of the right (left) cut and is $-i$ ($+i$) for the bottom of the right (left) cut. As ω'' moves away from $-\delta$, $\arg[n]$ lies in $(-\frac{\pi}{2}, \frac{\pi}{2})$ and approaches 0 for $\omega'' > -\delta$, and $\arg[n]$ lies in $(-\frac{5\pi}{2}, -\frac{3\pi}{2})$ and approaches -2π for $\omega'' < -\delta$. One consequence of the preceding discussion is that $\cos[(\alpha + \alpha' - \psi - \psi')/2] \geq 0$ for all ω in the complex plane and is zero along the branch cuts. Geometric arguments of these observations are readily obtained.

Since $\cos[(\alpha + \alpha' - \psi - \psi')/2] \geq 0$, the real part n_R of n is nonnegative. In fact, $n_R > 0$ except at ω'_\pm , and one can rigorously argue that the limiting value is 0 as ω approaches either branch point. The plots for n_R (Figs. A1(c) and A2(c)) and $|n|$ (Figs. (A1(a) and A2(a)) are very similar, except that n_R appears to have steeper slopes near the infinite discontinuities associated with the other branch points ω_\pm . As $|\omega|$ increases without bound, n_R approaches unity. For $|\omega| \geq 4\omega_0$, $|n_R - 1| \leq .01$. On the other hand, n_I is approximately zero for ω away from the branch cuts (Figs. A1(d) and A2(d)), and $|n_I| \leq .01$ for $|\omega| \geq 4\omega_0$. Moreover, the infinite discontinuities of $|n|$ at ω_\pm also appear in n_I . Since Fig. A1(d) is clipped, the peaks in Fig. A2(d) give an indication of the discontinuities.

Similar to Figs. A1 and A2, Figs. A3 and A4 exhibit in three dimensions and in two dimensions

four aspects ($|T|$, $\arg[T]$, $\text{Re}[T]$, $\text{Im}[T]$) of the transmission coefficient. According to Eq. (65),

$$|T(\omega)| = \frac{2}{\sqrt{1 + |n(\omega)|^2 + 2|n(\omega)| \cos(\arg[n(\omega)])}}, \quad (\text{A5})$$

$$\arg[T(\omega)] = \arctan \left[\frac{-|n(\omega)| \sin(\arg[n(\omega)])}{1 + |n(\omega)| \cos(\arg[n(\omega)])} \right], \quad (\text{A6})$$

for ω not along the branch cuts.

By Table 1, $\arg[n]$ takes on the values $-\frac{5\pi}{2}$, $-\frac{3\pi}{2}$, $-\frac{\pi}{2}$, and $\frac{\pi}{2}$ along the tops and bottoms of the cuts, which implies that $\cos(\arg[n(\omega)]) = 0$ on the cuts. Further, $|n(\omega)|$ is given by Eq. (A4) on the cuts. Hence, $|T(\omega)|$ is well-defined and continuous over the complex plane with

$$|T(\omega)| = 2 \sqrt{\frac{a^2 - \omega_2^2}{\omega_3^2 - \omega_2^2}} \quad (\text{A7})$$

along the branch cuts. Letting $a \rightarrow \omega_2$ and $a \rightarrow \omega_3$ imply

$$\lim_{\omega \rightarrow \omega'_\pm} |T(\omega)| = 2 \quad \text{and} \quad \lim_{\omega \rightarrow \omega_\pm} |T(\omega)| = 0. \quad (\text{A8})$$

Figures A3(a) and A4(a) indicate that $|T|$ has maxima and minima at the branch points ω'_\pm and ω_\pm , respectively, and quickly approaches unity for ω away from the branch cuts.

Also because $\cos(\arg[\omega])$ is nonnegative in the complex plane and is zero on the cuts, the denominator in Eq. (A6) is positive. Thus $-\frac{\pi}{2} < \arg[T(\omega)] < \frac{\pi}{2}$, and $\arg[T(\omega)] = 0$ when ω lies along the line $\omega = -i\delta$ minus the branch cuts. Along the cuts,

$$\arg[T(\omega)] = \begin{cases} \text{Arctan} \left[-\sqrt{\frac{\omega_3^2 - a^2}{a^2 - \omega_2^2}} \right], & \text{Top Right \& Bottom Left Cuts} \\ \text{Arctan} \left[\sqrt{\frac{\omega_3^2 - a^2}{a^2 - \omega_2^2}} \right], & \text{Bottom Right \& Top Left Cuts.} \end{cases} \quad (\text{A9})$$

Clearly, the argument of T is discontinuous along each cut, except at $\omega = \omega'_\pm$ ($a = \pm\omega_3$) where $\arg[T(\omega)] = 0$. This discontinuous behavior directly reflects the discontinuities of $\arg[n(\omega)]$ along the cuts. Equation (A9) also implies that $\arg[T(\omega)] \rightarrow -\frac{\pi}{2}$ as $\omega \pm \omega_\pm$ along the top right and bottom left cuts and that $\arg[T(\omega)] \rightarrow \frac{\pi}{2}$ as $\omega \pm \omega_\pm$ along the bottom right and top left cuts. The π jumps in the argument of T at ω_\pm are borne out by the sharp inner edges of the two fin-like structures in Figs. A3(b) and A4(b).

From Eqs. (65) and Figs. A3(c) and A4(c), one can deduce that the real part T_R of $T(\omega)$ is continuous in the cut plane, that T_R can be made continuous along the cuts by defining it with Eq. (A7) at those points, that $0 \leq T_R(\omega) \leq 2$, and that the maximum (minimum) value 2(0) of T_R occurs at ω'_\pm (ω_\pm). Phenomena that are clearly visible in both figures include a ridge above each cut, peaks about ω'_\pm , valleys about ω_\pm , and a leveling off to the limiting value of 1 as ω moves away from the branch cuts.

On the other hand, the presence of the sine function makes T_I discontinuous along the branch cuts, except at points where the limiting value of T_I is 0. Analytically, one can show that $|T_I(\omega)| < 1$ off the cuts and that

$$T_I(\omega) = \begin{cases} \frac{2}{\omega_3^2 - \omega_2^2} \sqrt{(a^2 - \omega_2^2)(\omega_3^2 - a^2)}, & \text{Bottom Right \& Top Left Cuts} \\ -\frac{2}{\omega_3^2 - \omega_2^2} \sqrt{(a^2 - \omega_2^2)(\omega_3^2 - a^2)}, & \text{Top Right \& Bottom Left Cuts.} \end{cases} \quad (\text{A10})$$

Since $|T_I| < 1$ for ω not on the branch cuts and $|T_I| = 1$ only at $a = \pm[(\omega_3^2 + \omega_2^2)/2]^{1/2}$ along the top and bottom of each cut, clearly $-1 \leq T_I(\omega) \leq 1$ for all ω , $\pm[(\omega_3^2 + \omega_2^2)/2]^{1/2} - i\delta$ are maxima along the bottom right and top left cuts, and $\pm[(\omega_3^2 + \omega_2^2)/2]^{1/2} + i\delta$ are minima along the top right and bottom left cuts. This behavior is apparent in Fig. A4(d), where the dark curve approximates the bottom of the cuts [$\omega''/\omega_0 = -0.0701$ or $\omega'' \doteq -1.0014\delta$] and the light curve approximates the top of the cuts [$\omega''/\omega_0 = -0.0699$ or $\omega'' \doteq -0.9986\delta$]. As ω moves away from the cuts, T_I approaches unity.

According to Eqs. (20), $n(\omega)$ also determines the behavior of the reflection coefficient ($R = R_R + iR_I$). Figures (A5) and (A6) provide 3-D and cross-sectional graphs of three of the four aspects of $R(\omega)$. Plots of R_I are omitted since $R_I = T_I$ (see Figs. A3(d) and A4(d)). By Eq. (A4),

$$|R(\omega)| = \left[\frac{1 + |n(\omega)|^2 - 2|n(\omega)| \cos(\arg[n(\omega)])}{1 + |n(\omega)|^2 + 2|n(\omega)| \cos(\arg[n(\omega)])} \right]^{\frac{1}{2}}, \quad (\text{A11})$$

which reduces to unity as ω approaches the top or bottom of either cut. Therefore, setting $|R| = 1$ on the cuts insures that $|R|$ is continuous over the complex plane. Since $\cos(\arg[n(\omega)]) = 0$, if and only if, ω is on a side of one of the cuts, $|R|$ attains its maximum value of 1 only on the cuts. As $|\omega|$ increases, $|n| \rightarrow 1$ and $\arg[n] \rightarrow 0$ or -2π (Fig. A1(b) and Table 1). Consequently, the numerator in Eq. (A11), hence $|R|$, approaches 0 through positive values. These characteristics are discernible in Figs. A5(a) and A6(a).

The argument of R ,

$$\arg[R(\omega)] = \arctan \left[\frac{-2|n(\omega)| \sin(\arg[n(\omega)])}{1 - |n(\omega)|^2} \right], \quad (\text{A12})$$

has discontinuities not only along the branch cuts from the discontinuities of $\arg[n(\omega)]$ but also along the imaginary axis ($\omega' = 0$) stemming from the definition in Eq. (A12). This latter discontinuity is manifested as the wall-like structure in Fig. A5(b), which corresponds to a 2π jump. Unfortunately, the jump discontinuities along the cuts are hidden by the surface. To perceive them, look at the cross-sectional curves on either side of the line $\omega'' = -\delta$ (Fig. A6(b)). The light curve and the dark curve correspond to $\omega'' \doteq -0.9986\delta$ and $\omega'' \doteq -1.0014\delta$, respectively. As $\omega \rightarrow \omega_+$ on the top and bottom of the right cut, $\arg[R(\omega)] \rightarrow -\pi$ and π , respectively; while $\arg[R(\omega)] \rightarrow \pi$ and $-\pi$ as $\omega \rightarrow -\omega_+$ on the top and bottom of the right cut.

The real part R_R of the reflection coefficient is

$$R_R(\omega) = \frac{1 - |n(\omega)|^2}{1 + |n(\omega)|^2 + 2|n(\omega)| \cos(\arg[n(\omega)])}. \quad (\text{A13})$$

Since $\cos(\arg[n(\omega)]) \geq 0$, $|R_R| \leq 1$, with equality occurring at the branch points. Specifically, $R_R(\omega'_\pm) = 1$ and $R(\omega_\pm) = -1$. Moreover, R_R has removable discontinuities along the cuts; that is, R_R is definable along the cuts by taking

$$R_R(\omega) = R_R(a - i\delta) = \frac{2a^2 - \omega_2^2 - \omega_3^2}{\omega_3^2 - \omega_2^2} \quad (\text{A14})$$

for a in $[-\omega_3, -\omega_2]$ or $[\omega_2, \omega_3]$. Thus the arcs in Figs. A5(c) and A6(c) connecting the values of R_R at ω'_- and ω_- are segments of a parabola.

Of special interest is the behavior of $T(\omega(\theta))$ because of its role in determining the Sommerfeld precursor \mathcal{A}_S with Eq. (66). Recall that T_R and T_I are the factors in this equation and are evaluated at the distant saddle point ω_{D1} , which itself depends on θ . Table A1 provides values of T_R and T_I at the ω_{D1} and ω_{N1} of Tables 3 and 4. The evaluations at the near saddle points ω_{N1} are included for completeness. As θ increases from 1 to 20, $T_R(\omega_{D1}(\theta))$ monotonically increases, while $T_I(\omega_{D1}(\theta))$ is a negligible, positive number for each value of θ . In fact, T_I never exceeds 0.014. In the two limiting situations, $\theta \rightarrow 1+$ and $\theta \rightarrow +\infty$, the limiting values of $T_I(\omega_{D1}(\theta))$ are 1 and 2, respectively. These limits are obtained from Eqs. (65), Eqs. (19), and Fig. 2 by noting that

$$\lim_{\theta \rightarrow 1+} \cos[(\alpha + \alpha' - \psi - \psi')/2] = 1, \quad (\text{A15a})$$

$$\lim_{\theta \rightarrow 1+} \sin[(\alpha + \alpha' - \psi - \psi')/2] = 0, \quad (\text{A15b})$$

$$\lim_{\theta \rightarrow 1+} \frac{\rho\rho'}{rr'} = 1, \quad (\text{A15c})$$

$$\lim_{\theta \rightarrow +\infty} \frac{\rho\rho'}{rr'} = 0. \quad (\text{A15d})$$

Table A1 – Transmission Coefficients Evaluated at the Distant ($\omega_{D1}(\theta)$) and Near ($\omega_{N1}(\theta)$) Saddle Points, Where θ is Normalized Time

θ	$T(\omega_{D1}(\theta))$	$T(\omega_{N1}(\theta))$
1.000	1.0000 – 0.00000 <i>i</i>	0.8958 – 0.00000 <i>i</i>
1.009	1.0044 – 0.00007 <i>i</i>	0.8921 – 0.00000 <i>i</i>
1.010	1.0048 – 0.00008 <i>i</i>	0.8917 – 0.00000 <i>i</i>
1.015	1.0071 – 0.00014 <i>i</i>	0.8897 – 0.00000 <i>i</i>
1.020	1.0094 – 0.00020 <i>i</i>	0.8879 – 0.00000 <i>i</i>
1.025	1.0115 – 0.00027 <i>i</i>	0.8861 – 0.00000 <i>i</i>
1.030	1.0136 – 0.00034 <i>i</i>	0.8843 – 0.00000 <i>i</i>
1.040	1.0177 – 0.00048 <i>i</i>	0.8810 – 0.00000 <i>i</i>
1.050	1.0216 – 0.00062 <i>i</i>	0.8779 – 0.00000 <i>i</i>
1.100	1.0392 – 0.00129 <i>i</i>	0.8643 – 0.00000 <i>i</i>
1.150	1.0546 – 0.00190 <i>i</i>	0.8531 – 0.00000 <i>i</i>
1.200	1.0685 – 0.00246 <i>i</i>	0.8434 – 0.00000 <i>i</i>
1.250	1.0813 – 0.00296 <i>i</i>	0.8348 – 0.00000 <i>i</i>
1.300	1.0933 – 0.00343 <i>i</i>	0.8269 – 0.00000 <i>i</i>
1.400	1.1154 – 0.00429 <i>i</i>	0.8129 – 0.00000 <i>i</i>
1.500	1.1356 – 0.00505 <i>i</i>	0.8000 – 0.00000 <i>i</i>
1.502735905	1.1361 – 0.00507 <i>i</i>	0.7994 – 0.00000 <i>i</i>
1.510	1.1375 – 0.00512 <i>i</i>	0.7986 – 0.00047 <i>i</i>
1.520	1.1395 – 0.00519 <i>i</i>	0.7976 – 0.00073 <i>i</i>
1.530	1.1414 – 0.00526 <i>i</i>	0.7966 – 0.00091 <i>i</i>
1.540	1.1433 – 0.00533 <i>i</i>	0.7955 – 0.00106 <i>i</i>
1.550	1.1452 – 0.00540 <i>i</i>	0.7945 – 0.00119 <i>i</i>
1.600	1.1544 – 0.00574 <i>i</i>	0.7896 – 0.00168 <i>i</i>
1.700	1.1720 – 0.00638 <i>i</i>	0.7805 – 0.00231 <i>i</i>
1.800	1.1887 – 0.00696 <i>i</i>	0.7722 – 0.00276 <i>i</i>
1.900	1.2046 – 0.00751 <i>i</i>	0.7646 – 0.00311 <i>i</i>
2.000	1.2197 – 0.00801 <i>i</i>	0.7574 – 0.00340 <i>i</i>
2.500	1.2872 – 0.01002 <i>i</i>	0.7278 – 0.00435 <i>i</i>
3.000	1.3441 – 0.01140 <i>i</i>	0.7047 – 0.00493 <i>i</i>
4.000	1.4359 – 0.01284 <i>i</i>	0.6694 – 0.00562 <i>i</i>
5.000	1.5068 – 0.01323 <i>i</i>	0.6426 – 0.00602 <i>i</i>
10.000	1.7023 – 0.01094 <i>i</i>	0.5618 – 0.00677 <i>i</i>
20.000	1.8362 – 0.00688 <i>i</i>	0.4845 – 0.00692 <i>i</i>
100.000	1.9647 – 0.00162 <i>i</i>	0.3261 – 0.00591 <i>i</i>
1000.000	1.9964 – 0.00016 <i>i</i>	0.1689 – 0.00355 <i>i</i>
∞	2.0000 – 0.00000 <i>i</i>	0.0000 – 0.00000 <i>i</i>

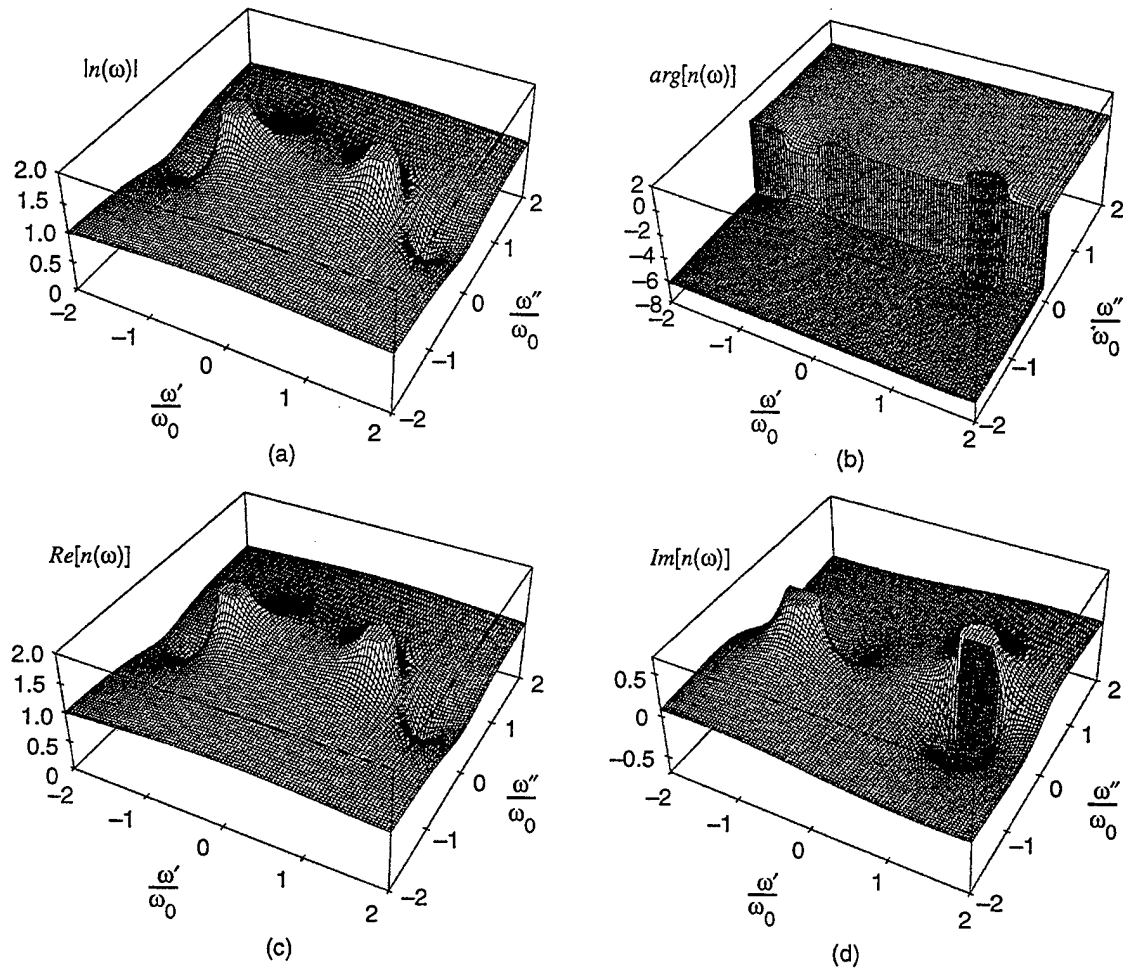


Fig. A1 – Refractive index n over the cut complex plane for a singly resonant Lorentz medium with $\omega_0 = 4.0 \times 10^{16} \text{ s}^{-1}$, $b^2 = 20.0 \times 10^{32} \text{ s}^{-2}$, and $\delta = 0.28 \times 10^{16} \text{ s}^{-1}$: (a) $|n(\omega)|$, (b) $\arg[n(\omega)]$, (c) $\text{Re}[n(\omega)]$, and (d) $\text{Im}[n(\omega)]$. The real (ω') and imaginary (ω'') axes are normalized by ω_0 .

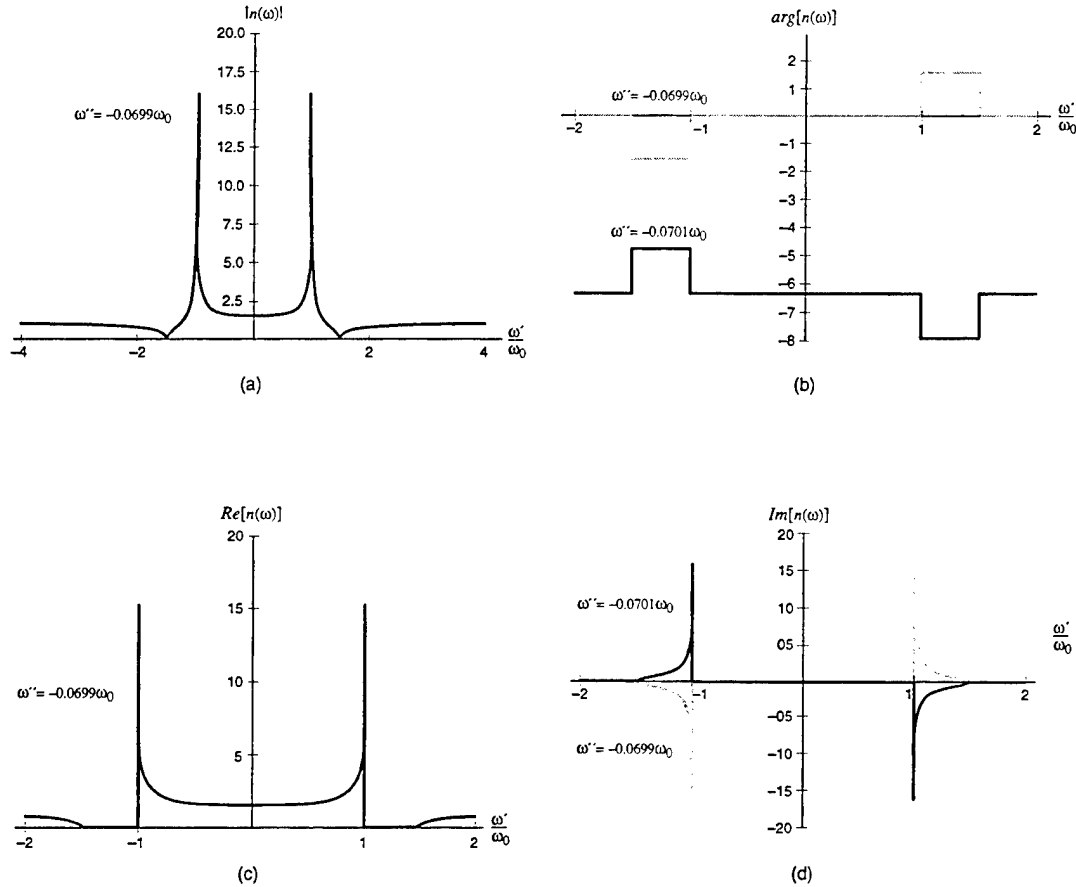


Fig. A2 – Cross-sectional views of the refractive index n for a singly resonant Lorentz medium with $\omega_0 = 4.0 \times 10^{16} \text{ s}^{-1}$, $b^2 = 20.0 \times 10^{32} \text{ s}^{-2}$, and $\delta = 0.28 \times 10^{16} \text{ s}^{-1}$: (a) $|n(\omega)|$ along $\omega'' = -0.0699\omega_0$, (b) $\arg[n(\omega)]$ along $\omega'' = -0.0699\omega_0$ (light curve) and $\omega'' = -0.0701\omega_0$ (dark curve), (c) $\text{Re}[n(\omega)]$ along $\omega'' = -0.0699\omega_0$, and (d) $\text{Im}[n(\omega)]$ along $\omega'' = -0.0699\omega_0$ (light curve) and $\omega'' = -0.0701\omega_0$ (dark curve). The real (ω') and imaginary (ω'') axes are normalized by ω_0 .

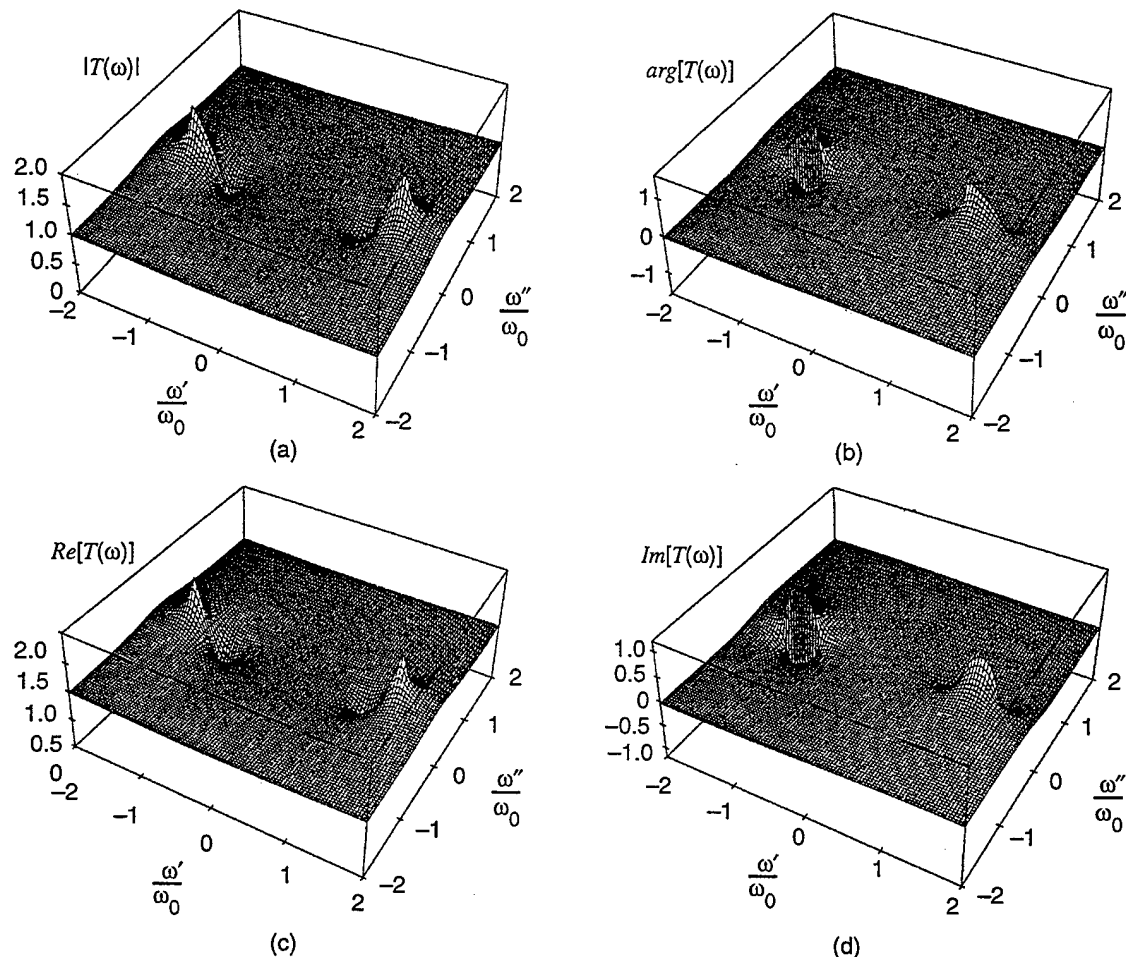


Fig. A3 – Transmission coefficient T over the cut complex plane for a singly resonant Lorentz medium with $\omega_0 = 4.0 \times 10^{16} \text{ s}^{-1}$, $b^2 = 20.0 \times 10^{32} \text{ s}^{-2}$, and $\delta = 0.28 \times 10^{16} \text{ s}^{-1}$: (a) $|T(\omega)|$, (b) $\arg[T(\omega)]$, (c) $\text{Re}[T(\omega)]$, and (d) $\text{Im}[T(\omega)]$. The real (ω') and imaginary (ω'') axes are normalized by ω_0 .

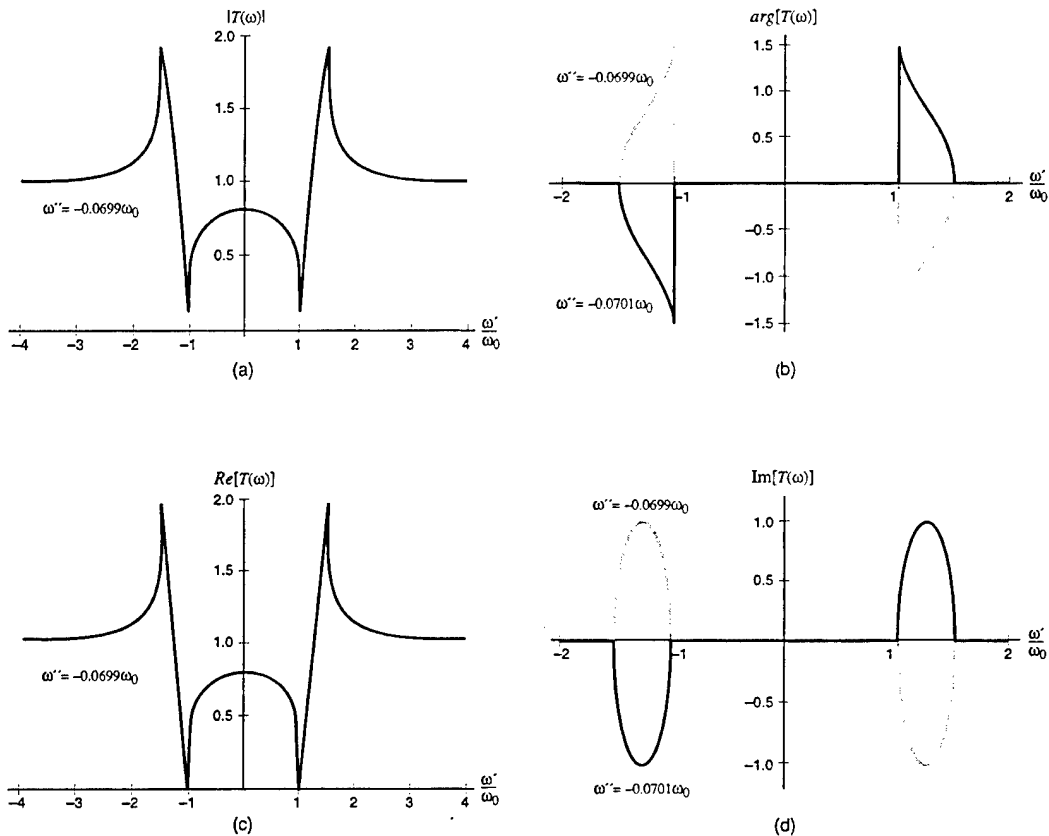


Fig. A4 - Cross-sectional views of the transmission coefficient T for a singly resonant Lorentz medium with $\omega_0 = 4.0 \times 10^{16} \text{ s}^{-1}$, $b^2 = 20.0 \times 10^{32} \text{ s}^{-2}$, and $\delta = 0.28 \times 10^{16} \text{ s}^{-1}$: (a) $|T(\omega)|$ along $\omega'' = -0.0699\omega_0$, (b) $\arg[T(\omega)]$ along $\omega'' = -0.0699\omega_0$ (light curve) and $\omega'' = -0.0701\omega_0$ (dark curve), (c) $\operatorname{Re}[T(\omega)]$ along $\omega'' = -0.0699\omega_0$, and (d) $\operatorname{Im}[T(\omega)]$ along $\omega'' = -0.0699\omega_0$ (light curve) and $\omega'' = -0.0701\omega_0$ (dark curve). The real (ω') and imaginary (ω'') axes are normalized by ω_0 .

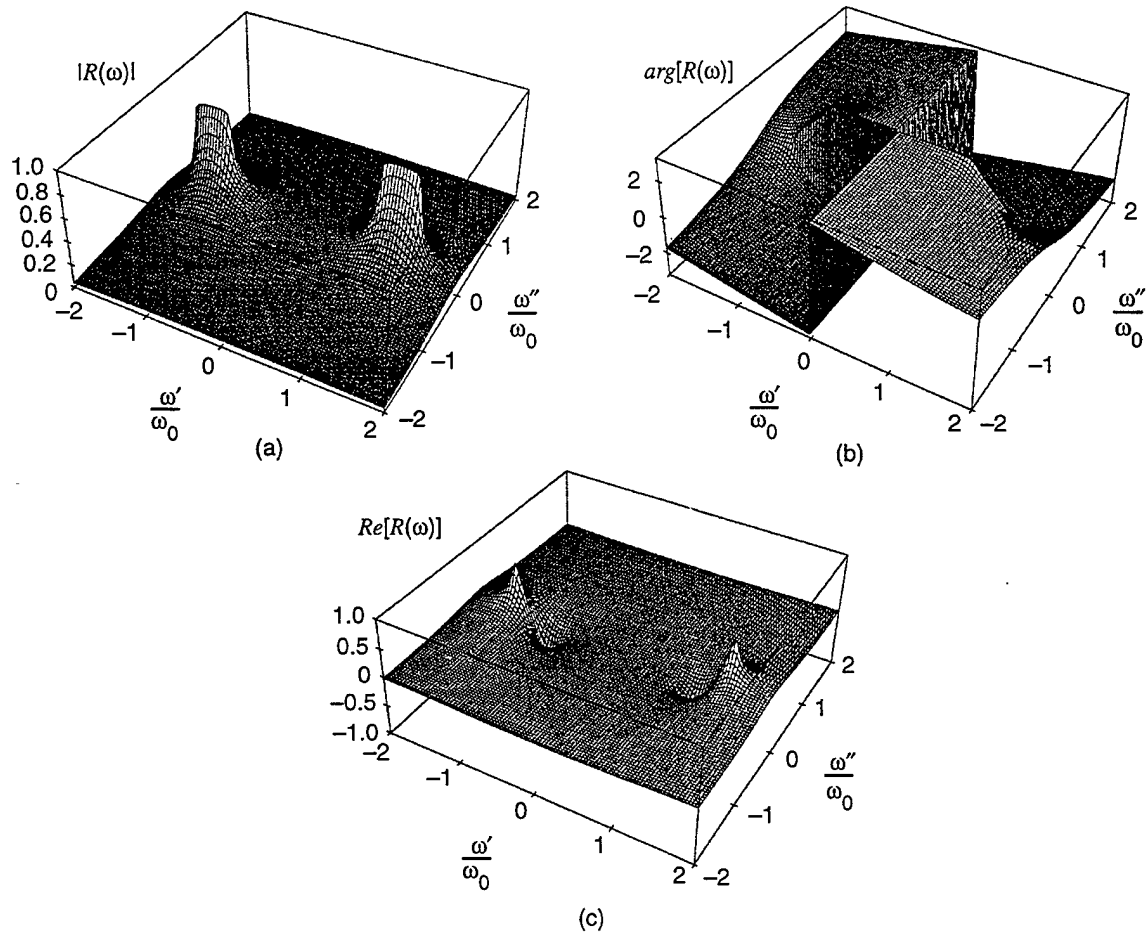


Fig. A5 – Reflection coefficient R over the cut complex plane for a singly resonant Lorentz medium with $\omega_0 = 4.0 \times 10^{16} \text{ s}^{-1}$, $b^2 = 20.0 \times 10^{32} \text{ s}^{-2}$, and $\delta = 0.28 \times 10^{16} \text{ s}^{-1}$: (a) $|R(\omega)|$, (b) $\arg[R(\omega)]$, (c) $\text{Re}[R(\omega)]$, and (d) $\text{Im}[R(\omega)]$. The real (ω') and imaginary (ω'') axes are normalized by ω_0 .

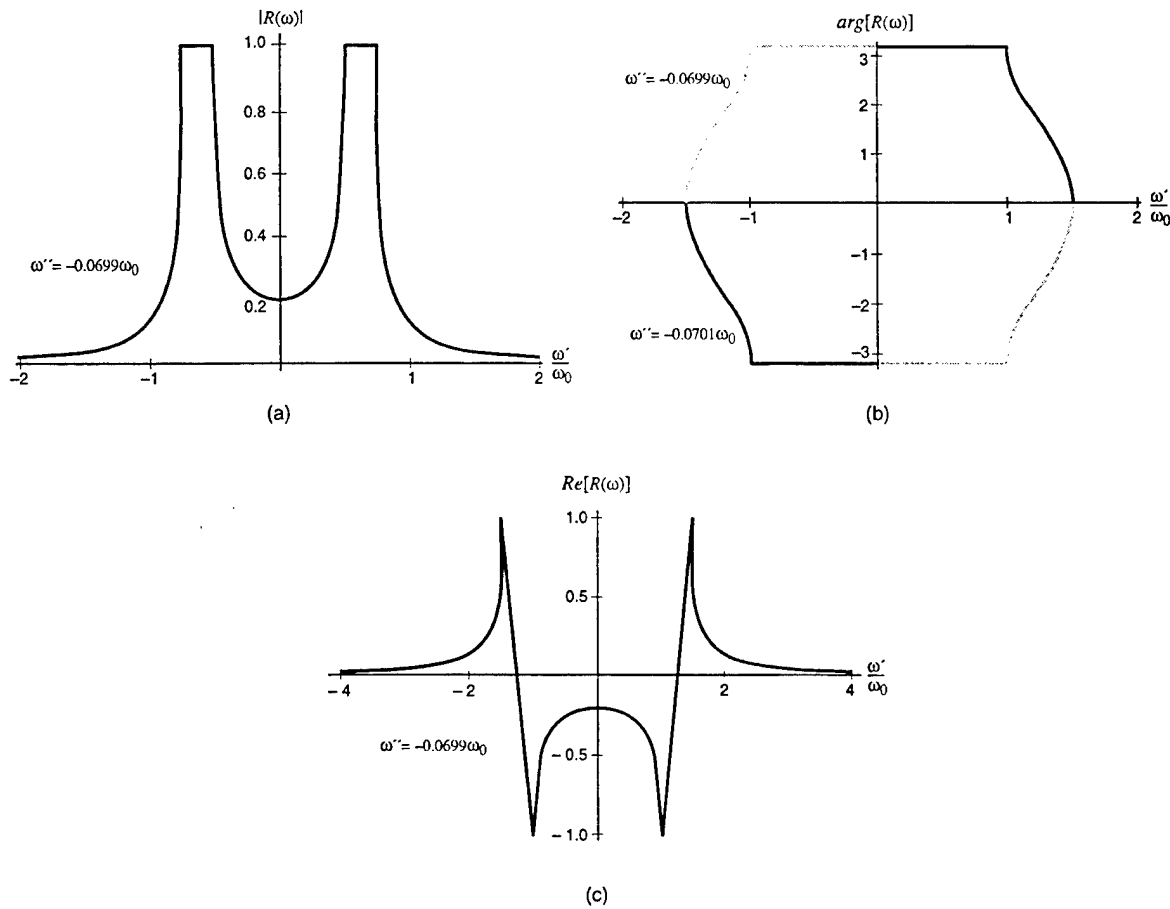


Fig. A6 – Cross-sectional views of the reflection coefficient R for a singly resonant Lorentz medium with $\omega_0 = 4.0 \times 10^{16} \text{ s}^{-1}$, $b^2 = 20.0 \times 10^{32} \text{ s}^{-2}$, and $\delta = 0.28 \times 10^{16} \text{ s}^{-1}$: (a) $|R(\omega)|$ along $\omega'' = -0.0699\omega_0$, (b) $\arg[R(\omega)]$ along $\omega'' = -0.0699\omega_0$ (light curve) and $\omega'' = -0.0701\omega_0$ (dark curve), (c) $\text{Re}[R(\omega)]$ along $\omega'' = -0.0699\omega_0$, and (d) $\text{Im}[R(\omega)]$ along $\omega'' = -0.0699\omega_0$ (light curve) and $\omega'' = -0.0701\omega_0$ (dark curve). The real (ω') and imaginary (ω'') axes are normalized by ω_0 .